Scatterometer Cross Calibration Using Volume Scattering Models for Amazon Rainforest Canopies

Evan Neil Chrisney

A thesis submitted to the faculty of
Brigham Young University
in partial fulfillment of the requirements for the degree of

Master of Science

David G. Long, Chair
Willie K. Harrison
Cameron K. Peterson

Department of Electrical and Computer Engineering

Brigham Young University

ABSTRACT

Scatterometer Cross Calibration Using Volume
Scattering Models for Amazon
Rainforest Canopies

Evan Neil Chrisney
Department of Electrical and Computer Engineering, BYU
Master of Science

Spaceborne scatterometers have measured the normalized radar cross section (RCS) of the earth's surface for several decades. Two frequencies, C- and Ku-band, have been used in designing scatterometers, such as with the Ku-band NASA Scatterometer (NSCAT) and the C-band Advanced Scatterometer (ASCAT). The scatterometer data record between C- and Ku-band has been disjoint for several decades due to the difficulties in cross calibration of sensors that operate at different frequencies and incidence angles. A model for volume scattering over the Amazon rainforest canopy that includes both the incidence angle and frequency dependence is developed to overcome this challenge in cross calibration.

Several models exist for the σ^0 incidence angle dependence, however, none of them are based on backscatter physics. This thesis develops a volume scattering model from a simple EM scattering model for cultural vegetation canopies and applies it to the volume scattering of the Amazon rainforest. It is shown that this model has lower variance than previously used models for the incidence angle dependence of σ^0, and also enables normalization of σ^0 with respect to the incidence angle.

In addition, the frequency dependence of σ^0 is discovered to be quite sensitive at Ku-band due to the distribution of leaf sizes in the Amazon rainforest. This may limit the accuracy of the model of the frequency dependence of σ^0. Although the proposed frequency dependence model may be limited for cross calibrating between C- and Ku-band, it provides the groundwork for future studies.

Keywords: NSCAT, ASCAT, scatterometer, calibration, volume scattering

ACKNOWLEDGMENTS

I give my first thanks to my family members for encouraging me to pursue complete my Master's degree. A special thanks goes out to my wife Mariana for her continued love and support throughout the years I've been in school. After many times of thinking I would not make it, she always reassured me that I was more than capable of finishing my thesis. I am also grateful for my professors in the Electrical and Computer Engineering department for pushing me past my intellectual limits over and over again. Without their help, I would not have been able to overcome the many rigorous challenges during my courses. I especially thank Dr. Peterson and Dr. Harrison of my graduate committee for reviewing my thesis. Most of all, I thank my advisor, Dr. Long, for his guidance during my years as a member of the MERS Lab. Thank you for the opportunity to work for you as a research assistant during both my undergraduate and graduate studies. Because of the opportunity you gave me, I was able to succeed in my classes and become confident in my abilities as an engineer.

TABLE OF CONTENTS

LIST OF FIGURES

CHAPTER 1. INTRODUCTION

Spaceborne scatterometers measure the normalized radar cross section (σ^0) of the Earth's surface. Although primarily designed for measuring wind vectors over the earth's oceans, σ^0 measurements have been used in many other geophysical applications, such as studies of vegetation, ice, and land [1]. Since such geophysical studies of the earth are very important, it is desirable that scatterometers are calibrated well.

This thesis develops a model for the backscatter observed from the Amazon rainforest applicable at mid-incidence angle and C- and Ku-bands. A model for the backscatter observed from the Amazon rainforest will assist in future calibration studies of σ^0 observed by separate sensors. Current calibration studies lack a physical model for the backscatter from the Amazon rainforest and use either first order polynomial fits or ad hoc methods [2, 5, 6]. Developing a physical model will increase the fidelity of future calibration studies, allow the calibration of σ^0 between sensors at various incidence angles, and can provide a method for calibrating between sensors at C- and Ku-bands.

This section introduces scatterometry and scatterometer design. Post-launch cross calibration using the Amazon rainforest as a calibration region is discussed, and the scattering properties of the Amazon rainforest are described. The problem statement regarding the model for backscatter of the Amazon rainforest is then discussed, and an outline of this thesis is given.

1.1 Scatterometer History

The two main architectures for the observation geometry of scatterometers are fan and pencil beam. The fan beam architecture utilizes several antennas which allows for observation of various incidence angles and a few fixed azimuth angles. The pencil beam architecture utilizes a rotating antenna which observes σ^0 at all azimuth angles and a fixed incidence angle. In addition, scatterometers have historically been designed in two different bands, C- and Ku-bands.

The first spaceborne scatterometer launched, Seasat, was a fan beam scatterometer designed by NASA in 1978 which operated in Ku-band at 14.6 GHz [5]. The NASA Scatterometer (NSCAT) was later designed by NASA in 1996 which was also a dual polarized (V and H) fan beam scatterometer in Ku-band at 13.995 GHz. Follow-on NASA scatterometers, such as SeaWinds on QuikSCAT (QSCAT) in 1999 and RapidScat in 2014, adopted the pencil beam architecture. The European Space Agency (ESA) continued to use the fan beam architecture when they designed ERS-1 (ESCAT) Scatterometer in 1991 and the Advanced Scatterometer (ASCAT) in 2007 [2]. ASCAT is a vertically polarized (V-pol) fan beam scatterometer which operates in C-band at 5.3 GHz. An example of the various scatterometers is shown in Fig. 1.1.

	SASS	ESCAT	NSCAT	SeaWinds	ASCAT	OSCAT	HY-2A
Frequency & Band	14.6 GHz (Ku)	5.3 GHz (C)	13.995 GHz (Ku)	13.4 GHz (Ku)	5.3 GHz (C)	13.515 GHz (Ku)	13.255 GHz (Ku)
Antenna Configuration	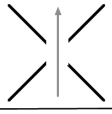	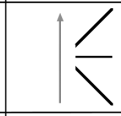	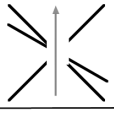	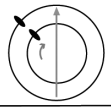	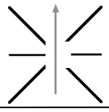	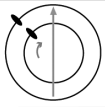	
Polarization	VV and HH	VV	VV, VV & HH, VV	VV-outer / HH-inner	VV	VV-outer / HH-inner	VV-outer / HH-inner
Beam Resolution	Fixed Doppler	Range gate	Variable Doppler	Pencil-beam	Range gate	Pencil-beam	Pencil-beam
Resolution (σ°)	nominally 50 km	50 km	25 km	Egg: 25x35 km Slice: 6x25 km	SZO: 25/50 km SZF: 4x20 km	Egg: 30x68 km Slice: 6x30 km	Inner: 23x33 km Outer: 26x37 km
Swath Configuration & Width in km	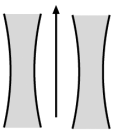		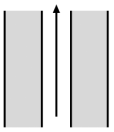	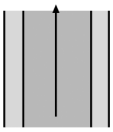	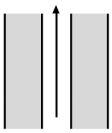	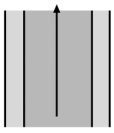	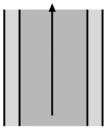
Incidence Angles	0° - 70°	18° - 59°	17° - 60°	46° & 54.4°	25° - 65°	49° & 57°	41° & 48°
Mission & Dates	SEASAT: 6/78-10/78	ERS-1:7/91-3/00 ERS-2:4/95-5/11	ADEOS-I: 8/96-6/97	QuikSCAT: 6/99-11/09* ADEOS-II: 1/02-10/02 RapidScat: 10/14-8/16	METOP-A: 6/07- METOP-B: 9/12-	OceanSat-2:10/09-2/14 ScatSat-1: 8/16-	HY-2A:8/11-

* continues operation in non-spinning mode

Figure 1.1: Various scatterometers are shown along with key parameters from 1978 to approximately 2014 [2]. In 2017, the OSCAT-2 scatterometer was launched with parameters similar to OSCAT.

With many scatterometer missions with differing observation geometries and operating frequencies, many studies calibrating and validating σ^0 measurements between different sensors have been performed.

1.2 Scatterometer Calibration

To ensure accurate σ^0 measurements for scientific studies, post launch cross calibration (hereafter referred as just calibration) is performed [6, 7]. Previous calibration studies of σ^0 have evaluated the incidence angle dependence over a wide variety of surfaces, such as the Amazon rainforest, the Sahara desert, and open oceans [8–10]. However, investigations at mid-incidence angle are limited on the frequency dependence of σ^0 between C- and Ku-bands.

A model for the frequency dependence of σ^0 at mid-incidence angle is developed and compared to observed ASCAT and NSCAT σ^0 over the Amazon rainforest. ASCAT and NSCAT are used because their geometries cover a similar range of incidence angles, and they operate in C- and Ku-bands, respectively.

The Amazon rainforest is an isotropic region that exhibits mainly volume scattering from the canopy crown, making it an ideal calibration region. The large depth of the canopy also allows for favorable properties in simplifying volume scattering models to a singular scattering model, i.e., accounting only for scattering from leaves, and ignoring surface scattering and multiple scattering from the trunk and ground floor. Since this model is fit to scatterometer data which has a resolution of roughly 10 km, it is only suited for use in applications greater than or equal to 10 km resolution. For higher resolution applications such as a synthetic aperture radar (SAR) scatterometer, the model is not applicable. A few key assumptions made in the scattering model, such as leaves being the only scattering mechanism and ignoring multiple scattering, are not valid for SAR in either C- or Ku-bands.

The development of a model for the frequency dependence of σ^0 at mid-incidence angle over the Amazon rainforest increases the fidelity of calibration studies for future scatterometer missions, since current calibration of σ^0 between different incidence angles does not use a physics based scattering model. Previous models include a 1st order polynomial fit between σ^0 and the incidence angle as well as γ^0, which normalizes σ^0 by the cosine of the incidence angle [2]. The physics-based scattering model is shown to have lower variance than both models in addition to being theoretically based instead of an ad hoc method. This model also allows calibration of σ^0 between C- and Ku-bands for the first time.

1.3 Thesis Statement

This thesis provides a simple volume scattering model for use in calibration of σ^0 between scatterometers of different frequencies and incidence angles over volume scattering regions, such as the Amazon rainforest. The model is derived independent of previous studies and arrives at a similar conclusion that volume scattering from a forest region with a large canopy depth is mainly from the canopy crown. The two-way transmitivity (Υ^2), which accounts for the transmission through the Amazon rainforest canopy, is defined. Since Υ^2 is found to be very close to 0 at both C- and Ku-bands, surface scattering can be ignored at both of these bands.

The frequency dependence of σ^0 for a volume scattering canopy is contained in the albedo, which can be empirically derived using a scattering model for leaves. This scattering model does not need to be perfect, but just sufficiently accurate to a few tenths of a dB. At scatterometer resolution, a simplified volume scattering model from leaves is appropriate. The extinction and absorption coefficients derived from the scattering model are used to estimate the albedo frequency dependence between C- and Ku-bands. Due to the distribution of leaf radii used in this thesis, a dip is found near Ku-band in the σ^0 frequency dependence model. This suggests that σ^0 is highly sensitive to frequency in this band, which may also explain why NSCAT σ^0 are approximately 1 dB higher than QSCAT σ^0 although they are separated by only 500 MHz. Although this sensitivity unfortunately suggests that this model is limited for cross-calibration of σ^0 from C-band to Ku-band, it does give insight into the sensitivity of σ^0 with respect to frequency.

1.4 Thesis Motivation

The motivation for this thesis is to develop a model for calibrating scatterometers that operate at differing incidence angle and/or frequencies. The NASA scatterometer Climate Record Pathfinder (SCP) contains two disjoint data sets of scatterometer images in C- and Ku-bands from several sensors. With a working model to cross calibrate between C- and Ku-bands, these disjoint data sets can be joined into a multi-decade data set spanning almost 40 years. Even if a working model for cross calibration between C- and Ku-bands is not feasible based on the results of this thesis, the groundwork provided in this thesis for this research will lead to more insight into an area of calibration research which has never been done before.

However, this model is useful for the correction of the σ^0 incidence angle dependence, resulting in improved radar images over the Amazon rainforest region and permitting better intra-sensor calibration. By evaluating the accuracy of incidence angle and frequency dependence models, this research supports future calibration efforts.

1.5 Thesis Organization

Chapter 2 provides essential background information on the NSCAT and ASCAT sensors, the Amazon rainforest, and scatterometer calibration. Chapter 3 develops a model used for calibrating scatterometers of different incidence angles. Chapter 4 further develops this model for to explain the frequency dependence of σ^0, and also introduces the polarization dependence of σ^0. Chapter 5 entails the conclusion of this thesis. Appendix A discusses the spatial gradient of the Amazon rainforest mask and its suitability for use in calibration using QSCAT data. The azimuth modulation of σ^0 observed by the Indian Space Agency Scatsat Scatterometer (OSCAT-2) over the Amazon rainforest over the same region is explored, and the azimuth bias is shown to be instrumental and not stem from the spatial gradient of the mask.

CHAPTER 2. BACKGROUND

This section provides background information for technical content in subsequent chapters by describing the ASCAT and NSCAT scatterometers, the Amazon rainforest as a calibration region, and scatterometer calibration.

2.1 ASCAT

The Advanced Scatterometer (ASCAT) is an active microwave remote sensor that both transmits and receives vertically polarized (V-pol) microwave pulses. Although originally designed to observe ocean winds speeds, ASCAT has been applied to observe σ^0 of the Earth's surface in several ice and land applications [2].

Three ASCAT instruments have been launched by the European Space Agency (ESA) on the three Meteorological Operational (MetOp) satellites, A, B, and C. ASCAT is currently operated by the European organization for the exploitation of METerological SATellites (EUMETSAT). The MetOp A satellite is shown in Fig. 2.1. ASCAT is a C-band (5.255 GHz) fan-beam scatterometer with 6 antennas, all V-pol. There are two sets of three antennas on the left and right swaths, fore, mid and aft. The fore beam illumination patterns are located at 135 degrees, mid at 90, and aft at 45 degrees with respect to the ground track. This measurement geometry is shown in Fig. 2.2.

ASCAT orbits the earth in a sun-synchronous (polar) orbit. This allows almost full global coverage of σ^0 daily, with multiple passes over the polar regions. Since scatterometers are microwave instruments, they are able to penetrate through cloud cover at any time of the day, unlike optical instruments. This allows for creating radar images of σ^0 at any time, as seen in the NASA Scatterometer Climate Pathfinder project (SCP) available at scp.byu.edu.

Scatterometer Image Reconstruction (SIR) images and σ^0 measurements derived from these data sets are used in this thesis. The SIR algorithm was developed by the BYU Microwave Earth Remote Sensing (MERS) lab to enhance the resolution of scatterometer images. Specifi-

cally, level 1B data from ASCAT on MetOp A from the Amazon rainforest are used from January of 2007.

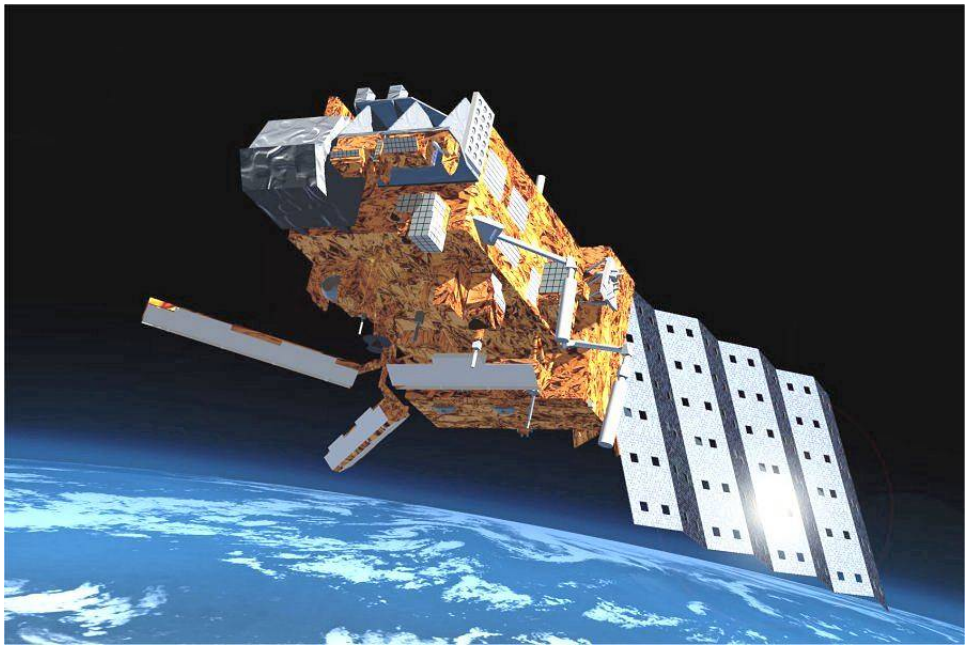

Figure 2.1: The MetOp A satellite which houses the ASCAT scatterometer. Picture adapted from [3].

2.2 NSCAT

The NASA Scatterometer NSCAT is also an active microwave remote sensor that both transmits and receives V-pol microwave pulses. NSCAT was launched on the Advanced Earth Observing Satellite (ADEOS), seen in Fig. 2.3. NSCAT was a Ku-band (13.995 GHz) fan-beam scatterometer with 8 beams. Unlike ASCAT, NSCAT does not have antennas positioned at the same relative azimuth angles in the left and right swaths. In addition, NSCAT has two antennas that are both (V-pol) and horizontally polarized (H-pol) antennas: 2 and 5 which are the center antennas of the right and left swaths, respectively. The right swath has 3 antenna beam patterns pointing at 45, 115, and 135 degrees. The left swath has 3 antenna beam patterns pointing at 45, 65, and 135 degrees.

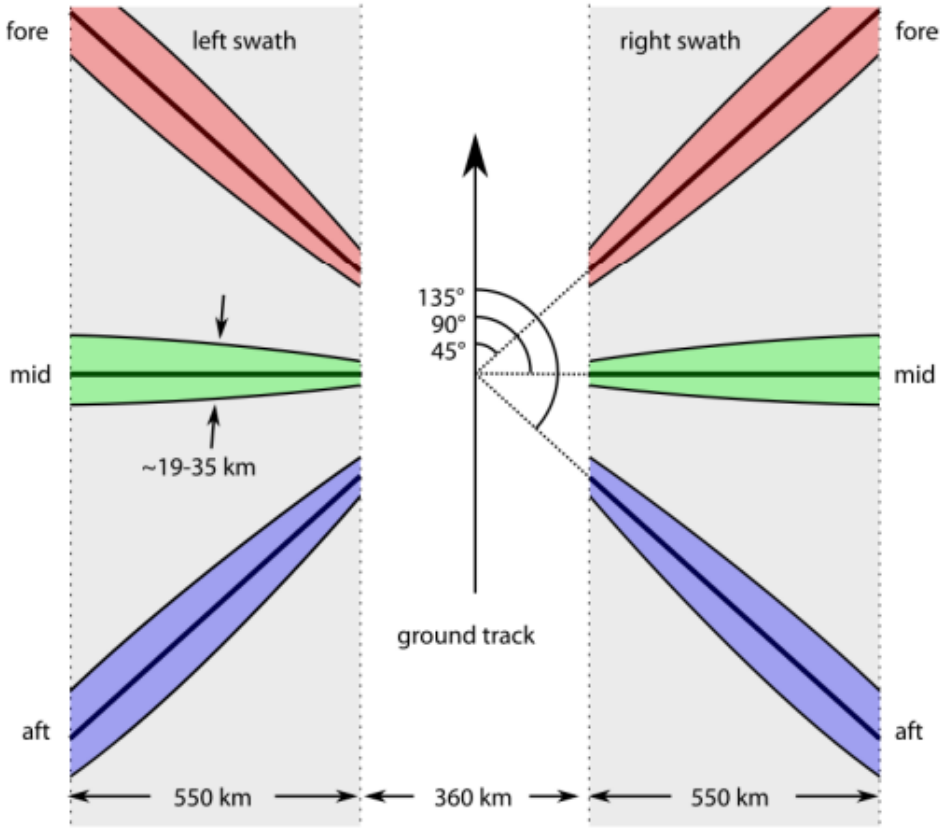

Figure 2.2: ASCAT measurement geometry

Similar to ASCAT, NSCAT operated in a polar orbit. Data and images are available from the NASA SCP project. Level 1.5 data from NSCAT observed from the Amazon rainforest in January 1997 are used in this thesis.

2.3 QuikSCAT

SeaWinds on QuikSCAT (QSCAT) is a dual-polarized (V and H) conically scanning pencil-beam scatterometer. This scatterometer observes σ^0 at fixed incidence angles for both V and H polarization. The success of the QSCAT mission over its 10 year data set makes it invaluable for cross calibration purposes. QSCAT was launched in 1999 following the end of the NSCAT mission in 1997. The NSCAT mission had an unfortunate premature end due to a malfunction in the solar panel system.

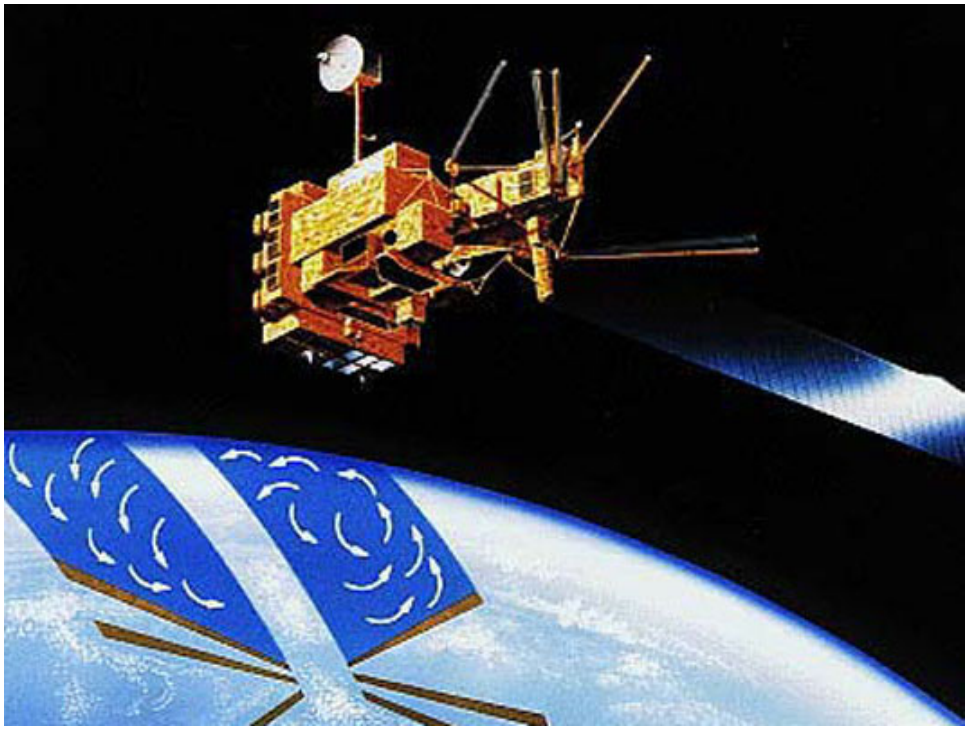

Figure 2.3: The ADEOS satellite which houses the NSCAT scatterometer. Picture adapted from [4].

QSCAT backscatter images from the NASA SCP project are used to create a binary mask over the Amazon rainforest, and level 1B data are used in Appendix A to investigate the utility of the Amazon rainforest mask as a calibration region.

2.4 Calibration Region

The Amazon rainforest has been used as a calibration region for scatterometers extensively due to its unique scattering properties [6, 8, 12, 13]. The Amazon rainforest is composed of a dense canopy layer that exhibits mainly volume scattering. It is isotropic with respect to azimuth angle, i.e; the backscatter is uniform in all azimuth directions, is spatially homogeneous, and does not vary significantly with season of year. It exhibits small diurnal changes due to the dew drying on the leaves throughout the day [13].

The Amazon rainforest is utilized as a calibration region for σ^0 from ASCAT and NSCAT by spatially selecting or masking measurements over homogeneous areas of the region. The many

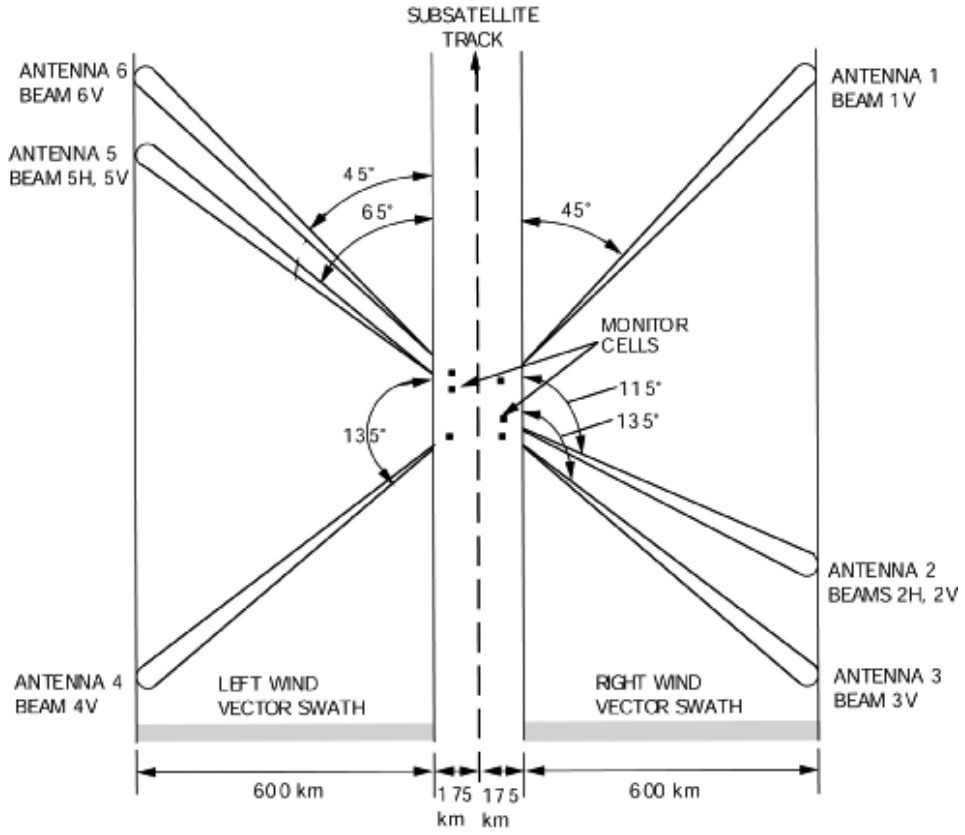

Figure 2.4: NSCAT measurement geometry

forming rivers and tributaries of the Amazon have much different scattering properties than the canopy, and are masked out using a binary masking method [10, 12]. High resolution SIR images contain σ^0 values for the Amazon rainforest, and the mean σ^0 is determined. Pixels that are within 1 dB of the mean σ^0 with a standard deviation ≤ 0.5 dB are included in the mask, are those that do not fit the criteria are flagged as 0, or binary masked out. Pixels that fall under the criteria are flagged as 1 and are considered homogeneous areas that exhibit mainly volume scattering. This mask is shown in Fig. 2.5.

This masked area is not a perfect calibration region; it contains a small spatial gradient of σ^0, and exhibits some diurnal variation [13]. A detailed description of the spatial gradient is given in Appendix A, where it is shown that the spatial gradient does not introduce any biases in QSCAT data with respect to azimuth angle. Therefore, we still consider the mask to be isotropic with respect to azimuth angle and suitable as a calibration region. This spatial gradient may stem

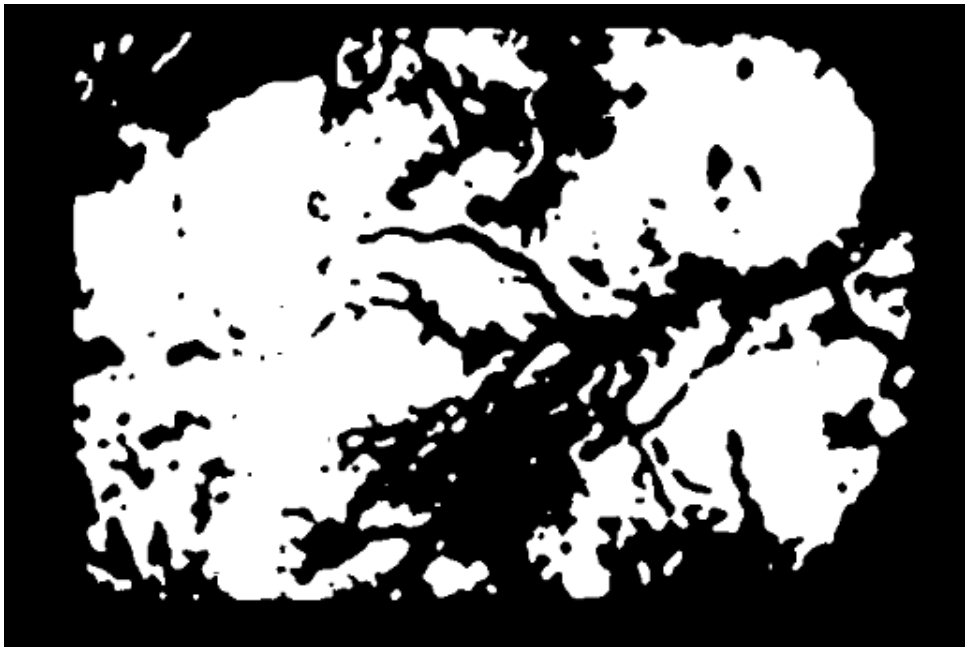

Figure 2.5: The binary mask of the Amazon rainforest derived from QSCAT SIR images. Only pixels that are within 1 dB of the mean σ^0 of the entire region with a standard deviation of less than or equal to 0.5 dB are included. These pixels are considered isotropic with respect to azimuth angle and exhibit volume scattering.

from the varying leaf sizes in the Amazon rainforest, as described by Malhado et al. [23]. Areas with larger leaf sizes in Malhado's study correspond with the spatial gradient of the masked area.

Although the bulk scattering properties of the Amazon rainforest at C- and Ku-band have been studied extensively [2, 5–8, 12–14], models for the scattering of the Amazon rainforest at C- and Ku-band are limited. Such models are more difficult to develop than models of other surfaces such as cultural vegetation and open oceans [15].

By assuming the scattering of the Amazon rainforest is due to a random but dense canopy layer and a rough surface beneath the canopy, a simple electromagnetic (EM) scattering model can be developed to describe the radar scattering. An EM scattering model developed for cultural vegetation can be adapted to scattering from the Amazon rainforest as

$$\sigma^0 = \sigma_s^0 \Upsilon^2 + \sigma_v^0 (1 - \Upsilon^2), \tag{2.1}$$

where Υ^2 is the two-way transmitivity of the canopy, σ_s^0 is the surface backscatter, and σ_v^0 is the canopy volume backscatter [15]. A similar EM model adapted for the surface and volume backscatter of sea ice is given by Swift as

$$\sigma^0 = \sigma_s^0 + \sigma_v^0, \tag{2.2}$$

where σ_s^0 and σ_v^0 are the surface and volume backscatter from sea ice [16]. In both of these models, the surface and volume backscatter components are independent random processes such that the modeled cross section is the incoherent sum of the two. It is shown in Chapter 3 that the surface scattering is negligible for the Amazon rainforest canopy, so only volume scattering contributes to the modeled cross section. For both models, the volume backscatter is

$$\sigma_v^0 = \frac{N_v \sigma^{back} cos(\theta)}{2\kappa_e}, \tag{2.3}$$

where σ_v^0 is the volume scattering coefficient, N_v is the scatterer number density, σ^{back} is the backscattering cross section of a single particle, and κ_e is the extinction coefficient. By ignoring multiple scattering,

$$\sigma_v^{back} = N_v \sigma^{back}, \tag{2.4}$$

where σ_v^{back} is the volume backscattering coefficient [15, 16]. If the scatterers in the volume are isotropic scatterers, then

$$\sigma_v^{back} = \sigma_v^{bist} = \kappa_s, \tag{2.5}$$

where σ_v^{bist} is the volume scattering coefficient, and κ_s is the scattering coefficient. In this isotropic scattering case, the volume backscattering coefficient is now

$$\sigma_v^0 = a\frac{cos(\theta)}{2}, \tag{2.6}$$

where $a = \frac{\kappa_s}{\kappa_e}$ is the single scattering albedo [15, 16]. If the scatterers in the volume not isotropic scatterers, then the scattering pattern is not uniform along all directions. Therefore $\sigma_v^{back} \neq \sigma_v^{bist}$, $\sigma_v^{back} \neq \kappa_s$, and Eq. 2.3 must be used.

The canopy of the Amazon rainforest is isotropic with respect to azimuth angle, and the scattering pattern for the entire canopy layer at scatterometer resolution is assumed uniform in all directions. In Chapter 3, Eq. 2.6 is developed, and in Chapter 4, both Eq. 2.3 and Eq. 2.6 are applied describe the volume scattering of the Amazon rainforest canopy.

The cultural vegetation model (Eq. 2.1) includes scattering from a canopy layer and a soil surface. It requires knowledge of the properties of the vegetation, such as the gravimetric moisture content, dielectric constant, canopy height, leaf size index, and more [15].

Although some of these properties may be known for specific regions of the Amazon such as the Anavilhanas flooded region along the lower Negro River [14], these properties are not known to a similar degree of fidelity for the extended Amazon rainforest region. Some challenges of determining these properties include the diversity of vegetation, diurnal and seasonal variations, and the large size of the Amazon rainforest. Although such parameters are not known for the full Amazon rainforest, the general properties of scattering can be adopted from models of broadly similar characteristics.

2.5 Scatterometer Cross Calibration

Classic methods of post-launch scatterometer calibration include calibrating wind vector measurements of the ocean to in situ measurements and numerical weather predicted winds [9], and calibration using land regions [30].

There are different classes of calibration using land targets, specifically intra-calibration and inter-calibration. Intra-calibration involves calibrating the σ^0 measurements of a sensor to itself. A corner reflector is impractical for calibration since a corner reflector consistent with 10 km scatterometer resolution is too large to be feasible. Therefore, large regions such as the rainforest are used for calibration. However, this region does not have a known true σ^0 response, so intra-calibration is not feasible. Therefore inter-calibration, or comparing σ^0 between various sensors, is more performed.

Inter-calibration of σ^0 between sensors has its own advantages and disadvantages. Inter-calibration is feasible between sensors of similar properties, such as observed incidence angle, geometry (fan-beam or pencil-beam), frequency, polarization, and local time of day observation. However, sensors such as ASCAT, NSCAT, and QSCAT all differ in these parameters. ASCAT

is in C-band, while NSCAT and QSCAT are both Ku-band but are fan-beam and pencil-beam instruments, respectively. All three of these instruments observe σ^0 at different local times of day over the Amazon rainforest [13].

2.6 Summary

The ASCAT and NSCAT scatterometers are fan-beam scatterometers. Their data are used in this thesis. The QSCAT scatterometer is a rotating pencil-beam scatterometer. Its data are used in Appendix A. The Amazon rainforest is used as a land calibration region, and a binary mask is created to use scatterometer data over homogeneous and isotropic regions that exhibit volume scattering. Two types of post-launch scatterometer calibration include intra- and inter-calibration. Inter-calibration involves comparing σ^0 between various sensors and is feasible; however, sensor observations differences such as incidence angle and polarization need to be considered.

CHAPTER 3. VOLUME SCATTERING MODEL

This chapter develops the volume scattering model in Eq. 2.1 and applies it to the volume scattering of the Amazon rainforest canopy. This model can be used to cross-calibrate σ^0 between scatterometers that observe σ^0 at difference incidence angles.

In order to apply Eq. 2.1 to the Amazon rainforest, Υ^2, as well as the extinction coefficient κ_e, must be developed. Υ^2 determines how much of an incident wave is transmitted through a layer and reflected back through the layer, while κ_e is the extinction within the layer due to scattering and absorption. In the following, it is shown that Υ^2 is negligible for the Amazon rainforest due to the dense canopy, so the semi-infinite canopy assumption in [15] is adopted and surface scattering from the ground layer is ignored.

3.1 Model Derivation

The transmitivity (Υ) accounts for loss due to transmission through a canopy at some incidence angle θ [15, 17]. The two-way transmitivity (Υ^2) accounts for the loss of σ^0 as the incident wave scatters through a canopy as well as loss back through the canopy from the backscatter.

Υ^2 is defined as

$$\Upsilon^2 = e^{-2\kappa_e sec(\theta)d}, \tag{3.1}$$

where κ_e is the extinction coefficient of the canopy layer, θ is the incidence angle of the transmitted (and reflected) wave, and d is the thickness of the canopy layer [15, 18].

The depth of the Amazon rainforest canopy d is estimated as 25m from altimeter measurements by Helmer et al. [19]. They observed Amazon basin lands with a minimum of 75 percent tree coverage yielded altimeter measured canopy heights with a mean of roughly 25 m.

Another study by Wang et al. gathered field data measurements of trees in the Anavilhanas region in the lower Negro River of the Amazon [14]. They used a least squares regression mapping

"diameter at breast height" (dbh) measurements of tree trunks to canopy heights and canopy depths,

$$Y = A + B\left(log_{10}(dbh)\right). \tag{3.2}$$

In their regression, canopy heights with dbh > 7 cm were used, and canopy depths with dbh > 2 cm were used. For canopy heights, $A = 22.31, B = 11.93$ with $r^2 = 0.49, n = 1967$ and for canopy depths, $A = 16.94, B = 11.93$ with $r^2 = 0.59, n = 1967$. They also measured the height of trees in the upper canopy layer ranging from 15 to 30 m, agreeing with the mean height of 25 m measured by Helmer et al. [19].

The Anavilhanas region field data from Helmer et al. may not be represented in our data set since most rivers are tributaries that are binary masked out [12]. However, the regression in Eq. 3.2 may be used to map tree heights of 25 meters as measured by Helmer et al. to an equivalent canopy depth. Assuming 25 m as the canopy height of the data mask yields a dbh of approximately 1.685 m using Eq. 3.2, which in turn yields a canopy height of roughly 19.5 m. Assuming a more conservative canopy height of 15 m (the minimum height of the upper canopy layer in the Wang study) yields a dbh of 25 cm and a canopy depth of 10.06 m. Given the wide range of measurements of the canopy height in both the Helmer and Wang studies, we conservatively model κ_e for a range of canopy depths from 5 m to 25 m.

3.1.1 Extinction Coefficient κ_e

Studies and measurements of κ_e for the Amazon rainforest canopy are limited. However, studies and measurements for κ_e for different forests and foliage such as deciduous [11] and aspen [20] are available.

Helicopter mounted scatterometer observations of κ_e of aspen foliage by Pitts et al. estimated that κ_e for aspen foliage is between 2.5 and 5.0 with a 70% confidence interval for canopy heights of mean 23.7 m [20]. Aspen foliage does not have quite the same attenuation properties of the Amazon canopy. However, with a similar canopy height of around 25 m and canopy depth of roughly 19.5 m, the Amazon canopy layer is expected to exhibit at least comparable attenuation of an incident EM wave. Measurements of κ_e from the aspen canopy are shown in Fig. 3.1 (a). Esti-

mated values of κ_e from two different models from empirical observations over deciduous foliage (described below) are shown.

Two Models for κ_e

A study by Currie et al. examined the one-way and two-way attenuation of deciduous canopies from 10 - 95 GHz, and citing other studies of attenuation at lower frequencies ranging from 100 MHz to 3 GHz. Two models for κ_e as a function of frequency for deciduous foliage from Currie et al. include a logarithmic model and a power law model [11, 21]. The logarithmic model is defined as

$$\kappa_e = a + b\left(log_{10}(F)\right), \tag{3.3}$$

where a and b are coefficients fit to empirical data, and F is frequency in GHz. The resulting coefficients in the deciduous foliage penetration experiment are $a = 1.102$ and $b = 1.48$. The power law model is defined as

$$\kappa_e = sF^{\frac{3}{4}}, \tag{3.4}$$

where s is scalar fit to empirical data, and F is the frequency in GHz. This model is used in lower frequency experiments for data between 0.1 and 3 GHz, with the scalar s given as 0.25. The deciduous foliage in this experiment has more open space than in the logarithmic model fit experiments, resulting in lower measurements for κ_e than the κ_e measurements used in the logarithmic model [11]. In both models, κ_e is reported in dB/m.

A comparison of Υ^2 for both the logarithmic and power law models of κ_e to canopy depth and frequency is given in Figs. 3.1-3.2. Assuming a canopy depth of roughly 19.5 m, Υ^2 at C- and Ku-band is lower than -250 dB of for both the power law and logarithmic models of Υ^2. Even a very conservative estimate of the canopy height of 5 m yields transmitivity of at most -65 dB for both models. Since Υ^2 is approximately 0 in linear space in C- and Ku-band at reasonable heights for the Amazon rainforest canopy, the modeled σ^0 is dominated by volume scattering. This conclusion that even at C-band σ^0 is predominantly from volume scattering agrees well with the results of the Wang study in the flooded Anavilhanas region of the Amazon rainforest [14], as well as with Kuga et al. [22].

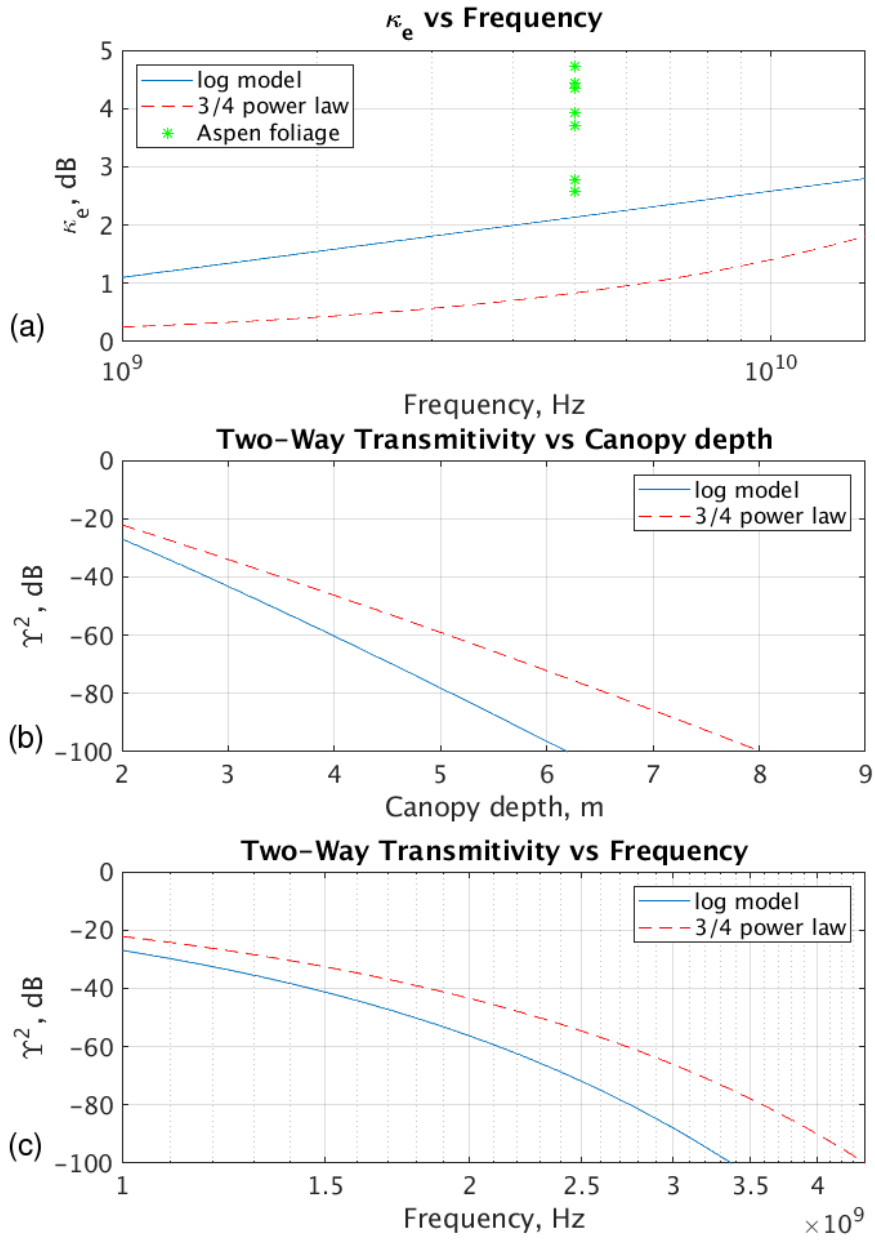

Figure 3.1: (a) κ_e versus frequency for two models of κ_e compared with empirical aspen foliage measurements. It is noted in (a) that κ_e is higher for the aspen foliage than the deciduous, nevertheless, both models are conservative estimates for our purposes. The power law model is consistently about 1 dB lower in κ_e than the logarithmic model. (b) A comparison is shown for Υ^2 versus canopy depth. The logarithmic model is between 5 dB at 2 m to 25 dB at 6 m lower than the power law model for Υ^2. (c) Υ^2 versus frequency. The power law model drops by about 20 dB per GHz from 1 to 5 GHz starting at -22 dB at 1 GHz, while the logarithmic model drops about 30 dB per GHz starting at -26 dB at the same frequencies.

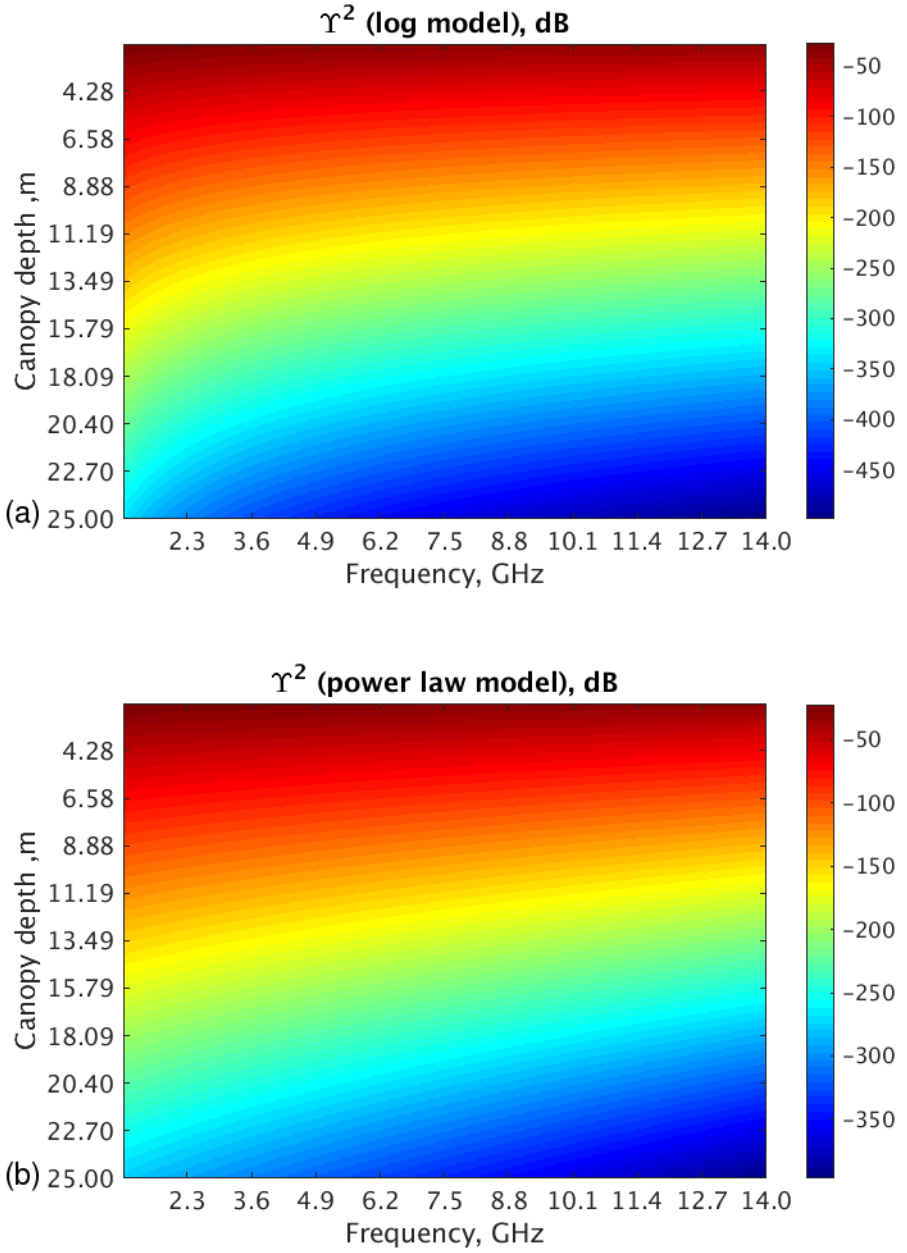

Figure 3.2: Υ^2 versus frequency and canopy depth for the logarithmic (a) and power law models (b) for κ_e (Eq. 4.20, 4.21). With the assumption that the canopy depth is 5 meters, there is roughly 86 dB of attenuation at 5.25 GHz and 100 dB of attenuation at 13.9 GHz. In (b), assuming a 5 meter canopy depth, there is roughly 64 dB of attenuation at 5.25 GHz, and 79 dB of attenuation at 13.9 GHz. We conclude that there is very little surface scattering at C- and Ku-band for backscattering over the Amazon rainforest canopy for both models of κ_e.

3.1.2 Leaf Sizes in the Amazon

Foliage in the Amazon rainforest has many different types of scatterers, including leaves, branches, vines, and other material in the canopy. Leaves are very abundant and the most studied of these scatterers. An examination of leaf size distributions to wavelengths in L-, C-, and Ku-bands is discussed below.

A study by Malhado et al. [23] provides a brief examination of leaf size distributions over various sites of interest in the Amazon rainforest. In their study, leaf size areas are categorized into 7 different classes. To compare these classes to sizes in wavelengths, each leaf is assumed to be round. Sizes in wavelength are compared to a radius given by the square root of the leaf size area divided by π. Results of the histogram converted into leaf radii is shown in Fig. 3.3. Although leaves are not the only scatterers in the Amazon rainforest canopy, leaves larger than the wavelengths at C- and Ku-band cause considerable volume scattering and restrict two-way surface scattering. This restriction yields a very low Υ^2 and a large two-way reflectivity.

The two-way reflectivity Γ^2,

$$\Gamma^2 = 1 - \Upsilon^2, \tag{3.5}$$

is very large at C- and Ku-band, confirming that the Amazon rainforest canopy has a very high volume scattering contribution at C- and Ku-band. Although Γ^2 approaches 1 at C- and Ku-band, L-band wavelengths are larger than 60% of the leaves in the Amazon rainforest canopy. Therefore, at lower wavelengths such as L-band, Γ^2 should be lower, and this is reasonable in the power law model for Υ^2. The power law model (Eq. 4.21) included frequencies in L-band in its empirical fit, while the logarithmic model (Eq. 4.20) for Υ^2 included frequencies in Ku-band and above. Although not ideal, these models provide a general idea of modelling Υ^2 at C- and Ku-band. It is shown in the next section that having an exact estimate for κ_e is not imperative in a volume scattering model as the scattering coefficient (κ_s), and inadvertently the albedo (a), can be solved for using least squares estimation.

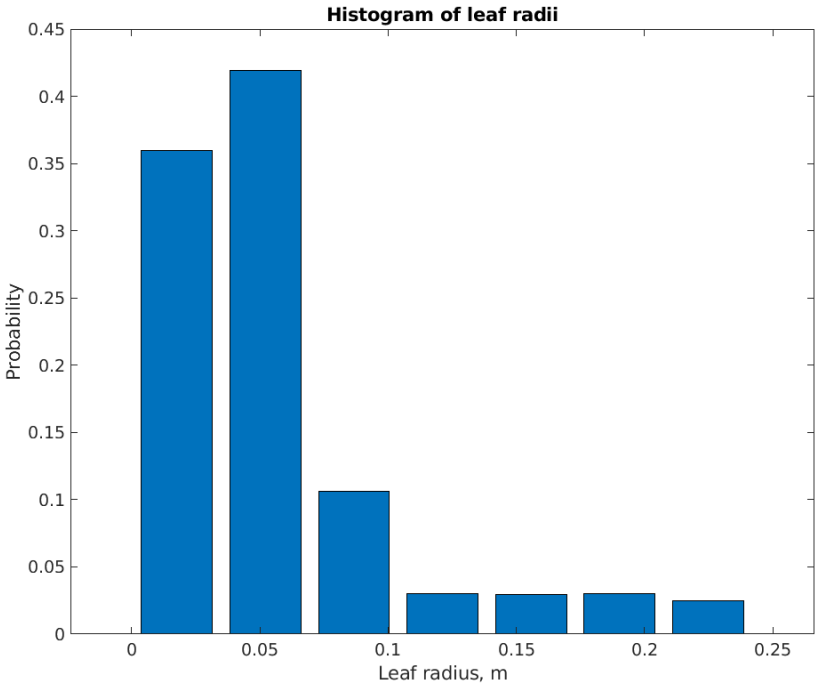

Figure 3.3: Using a circular area approximation for the area of a leaf, a leaf size distribution in meters for a sample in the Amazon rainforest adopted from [23] is shown. The leaf radii are binned into the 7 categories given by Malhado et al. [23]. The bin edges are 1.59 cm, 4.77 cm, 14.32 cm, 15.59 cm, 24.97 cm, 1.29 m, 1.37 m.

3.2 Volume Scattering Model

The σ^0 observed from the Amazon rainforest is written as

$$\sigma^0 = \sigma_s^0 \Upsilon^2 + \sigma_v^0 \left(1 - \Upsilon^2\right) + C_{offset}, \tag{3.6}$$

where σ_s^0 is the surface scattering contribution from the ground to the RCS, σ_v^0 is the volume scattering contribution from the canopy, and C_{offset} is an offset due to calibration. Since Υ^2 is approximately 0 at C- and Ku-band, Eq. 3.6 simplifies to

$$\sigma^0 = \sigma_v^0 + C_{offset}. \tag{3.7}$$

At C- and Ku-band, Υ^2 is approximately 0. However, at lower frequencies such as L-band this may not be true, and surface scattering cannot be ignored. Surface scattering for the Amazon rainforest is generalized to a relatively rough surface similar to the geometric optics model as in [14].

$$\sigma_s^0 = \frac{\Gamma_F(0)e^{-\tan^2(\theta_p)/(2r^2)}}{2r^2 cos^4(\theta_p)}, \tag{3.8}$$

where σ_s^0 is the scattering from the surface, $\Gamma_F(0)$ is the Fresnel reflection coefficient evaluated at normal incidence, θ_p is the incidence angle, and r is the rms surface slope [16, 24]. Parameters for the model such as the r and dielectric constant may be difficult to estimate, but the terms which rely on these parameters are lumped into some scalar such that

$$\sigma_s^0 = \frac{\Gamma_F(0)e^{0.5r^{-2}}}{2r^2}\frac{e^{-\tan^2(\theta_p)}}{cos^4(\theta_p)}, \tag{3.9}$$

or

$$\sigma_s^0 = g\vec{s}, \tag{3.10}$$

where $g = \frac{\Gamma_F(0)e^{0.5r^{-2}}}{2r^2}$ is a scalar, and $\vec{s} = \frac{e^{-\tan^2(\theta_p)}}{cos^4(\theta_p)}$ is a function of θ. The goal of modeling the scattering of the Amazon in this thesis is to avoid estimating the parameters in g, so we group them together as some scalar, but use the incidence angle in $\vec{s}$ for the surface scattering model.

The volume scattering term ${\sigma_v}^0$ is defined as

$${\sigma_v}^0 = \left(\frac{N_v\sigma^{back}}{2\kappa_e}\right)\cos(\theta_p), \tag{3.11}$$

where N_v is the scatterer number density, σ^{back} is the backscattering cross section per particle, and κ_e is the extinction coefficient [15, 16, 18]. In Chapter 2, we note that the Amazon rainforest is isotropic with respect to azimuth angle, or the backscatter is uniform in all directions. Although the individual scattering elements within the layer may not have an isotropic response (e.g. leaves), at the 5 km scatterometer footprint, the entire canopy layer has an isotropic response with respect to azimuth angle [12].

By assuming the canopy layer is an isotropic scatterer,

$$N_v\sigma^{back} = N_v\sigma^{bist} = \kappa_s, \tag{3.12}$$

where σ^{bist} is the bistatic cross section per particle, and κ_s is the scattering coefficient which is the scattering component of κ_e [15]. The single scattering albedo is

$$a = \frac{\kappa_s}{\kappa_e}. \tag{3.13}$$

The albedo describes how reflective a surface is. It is a dimensionless ratio between 0 and 1. An albedo of 0 would describe a surface that absorbs all radiation, and an albedo of 1 would describe a surface that reflects all radiation. Eq. 3.11 can be written as

$$\sigma_v{}^0 = \frac{\kappa_s}{\kappa_e}\vec{v}, \tag{3.14}$$

where $\frac{\kappa_s}{\kappa_e}$ is a scalar and $\vec{v} = \left(\frac{1}{2}\right)\cos(\theta_p)$ is a function of θ.

Using the newly defined surface and volume scattering terms, Eq. 3.6 becomes

$$\sigma^0 = \Upsilon^2 g\vec{s} + \frac{(1-\Upsilon^2)\kappa_s}{\kappa_e}\vec{v} + C_{offset}, \tag{3.15}$$

where we create the linear matrix equation

$$\sigma^0 = [\vec{s}\Upsilon^2, \frac{1-\Upsilon^2}{\kappa_e}\vec{v}, \vec{1}][g, \kappa_s, C_{offset}]^H, \tag{3.16}$$

where $\vec{1}$ is a column vector of 1's. For C- and Ku-band, Eq. 3.7 is

$$\sigma^0 = \frac{\kappa_s}{\kappa_e}\vec{v} + C_{offset}, \tag{3.17}$$

where we create the linear matrix equation

$$\sigma^0 = [\frac{1}{\kappa_e}\vec{v}, \vec{1}][\kappa_s, C_{offset}]^H. \tag{3.18}$$

We can further simplify Eq. 3.18 as the matrix equation

$$\mathbf{x} = \mathbf{Hb}, \tag{3.19}$$

where $\mathbf{x} = \sigma^0$ is an $n \times 1$ vector, $\mathbf{H} = [\frac{1}{\kappa_e}\vec{v}, \vec{1}]$ is an $n \times 2$ matrix, and $\mathbf{b} = [\kappa_s, C]^H$ is a 2×1 column vector. An estimate for $\mathbf{b}$ is solved for as

$$\hat{\mathbf{b}} = \mathbf{H}^{\dagger}\mathbf{x}, \tag{3.20}$$

where $\hat{\mathbf{b}} = [\hat{a}, \hat{C}]^T$ is an estimate of $\mathbf{b}$, and $\mathbf{H}^{\dagger}$ is a left psuedoinverse of $\mathbf{H}$.

The model for σ^0 is then

$$\hat{\mathbf{x}} = \mathbf{H}\hat{\mathbf{b}}, \tag{3.21}$$

where $\hat{\mathbf{x}}$ is an estimate for the modeled σ^0, and $\hat{\mathbf{b}}$ contains the parameters of the model.

We do not know $\mathbf{b}$, however our goal is not to estimate the parameters of $\mathbf{b}$, but rather to only estimate the model for σ^0 in Eq. 3.21. As discussed prior to this section, an exact estimate for κ_e is not necessary to solve for $\hat{\mathbf{b}}$ in Eq. 3.20 since κ_s is solved for using least squares. The albedo is the coefficient solved for in the least squares estimation, not κ_s. Any value of κ_e will result in an equivalent albedo, so it does not need to be used in the least squares estimate; alternatively, a κ_e of 1 may be used to solve directly for the albedo. The purpose of modeling κ_e was to show that the Amazon rainforest canopy was very dense and does not exhibit surface scattering in C- and Ku-band.

Using the SVD pseudoinverse yields the coefficients in $\mathbf{b}$ that minimize the least squared error of the fit $\mathbf{H}^{\dagger}$ to $\mathbf{x}$ [25]. A benefit of using the SVD pseudoinverse in the presence of zero mean Gaussian noise is that it yields unbiased estimates for both $\mathbf{b}$ and $\mathbf{x}$ in Eqs. 3.20 and 3.21, as discussed in the following section.

3.2.1 Noise Analysis of Volume Scattering Model

We assume there is some noise $\mathbf{n}$ that is Gaussian distributed with zero-mean and variance $\mathbf{R}$ such that

$$\mathbf{y} = \mathbf{x} + \mathbf{n}, \tag{3.22}$$

where $\mathbf{y}$ is the entire RCS σ^0 plus noise, $\mathbf{x}$ is the true signal model, and $\mathbf{n}$ is the noise. Since $\mathbf{n}$ is Gaussian distributed with zero-mean, we realize that $\mathbf{y}$ is also Gaussian distributed with mean $\mathbf{x}$

such that

$$f_a(\mathbf{y}) = \frac{(2\pi)^{-\frac{N}{2}}}{|\mathbf{R}|^{\frac{1}{2}}} \exp\left(-\frac{1}{2}(\mathbf{y}-\mathbf{x})^H \mathbf{R}^{-1}(\mathbf{y}-\mathbf{x})\right). \tag{3.23}$$

As in Eq. 3.20, the estimates for the scattering coefficient $\hat{\kappa_s}$ and the calibration offset $\hat{C}$ are contained in $\hat{\mathbf{b}}$. This is estimated using the pseudo inverse of $\mathbf{H}$, where the pseudo inverse of $\mathbf{H}$ using the singular value decomposition is given by

$$\mathbf{H}^{\dagger} = \mathbf{V}\Sigma^{-1}\mathbf{U}^H. \tag{3.24}$$

The estimate $\hat{\mathbf{b}}$ is then given by

$$\hat{\mathbf{b}} = \mathbf{H}^{\dagger}\mathbf{y}, \tag{3.25}$$

where it is realized that $\hat{\mathbf{b}}$ is Gaussian distributed with mean $\mathbf{b}$ and variance $\mathbf{R} = \mathbf{V}\Sigma^{-2}\mathbf{V}^H$. Since the expectation of $\hat{\mathbf{b}}$ is equal to $\mathbf{b}$, $E\{\hat{\mathbf{b}}\} = \mathbf{b}$, $\hat{\mathbf{b}}$ is an unbiased estimator for $\mathbf{b}$. If the variance of $\hat{\mathbf{b}}$ converges to 0 with many realizations of $\hat{\mathbf{b}}$, it is also a consistent estimator for $\mathbf{b}$.

The estimated signal and noise are given by

$$\mathbf{y} = \hat{\mathbf{x}} + \hat{\mathbf{n}}, \tag{3.26}$$

where $\hat{\mathbf{x}}$ is the signal estimate and $\hat{\mathbf{n}}$ is the noise estimate. The signal estimate is given by $\hat{\mathbf{x}} = \mathbf{H}\hat{a}$, or

$$\hat{\mathbf{x}} = \mathbf{P}_H\mathbf{y}, \tag{3.27}$$

where $\mathbf{P}_H$ is an orthogonal projection onto $\hat{\mathbf{x}}$. Using the orthogonal projection definition for the signal estimate, the noise estimate is $\hat{\mathbf{n}} = \mathbf{y} - \mathbf{P}_H\mathbf{y}$ or

$$\hat{\mathbf{n}} = (\mathbf{I} - \mathbf{P}_H)\,\mathbf{y}, \tag{3.28}$$

$$\hat{\mathbf{n}} = \mathbf{P}_A\mathbf{y}, \tag{3.29}$$

where $\mathbf{P}_A$ is an orthogonal projection onto $\hat{\mathbf{n}}$. The signal estimate $\hat{\mathbf{x}}$ is an unbiased estimator [26] for $\mathbf{x}$ since $E\{\hat{\mathbf{x}}\} = E\{\mathbf{H}\hat{b}\} = \mathbf{x}$.

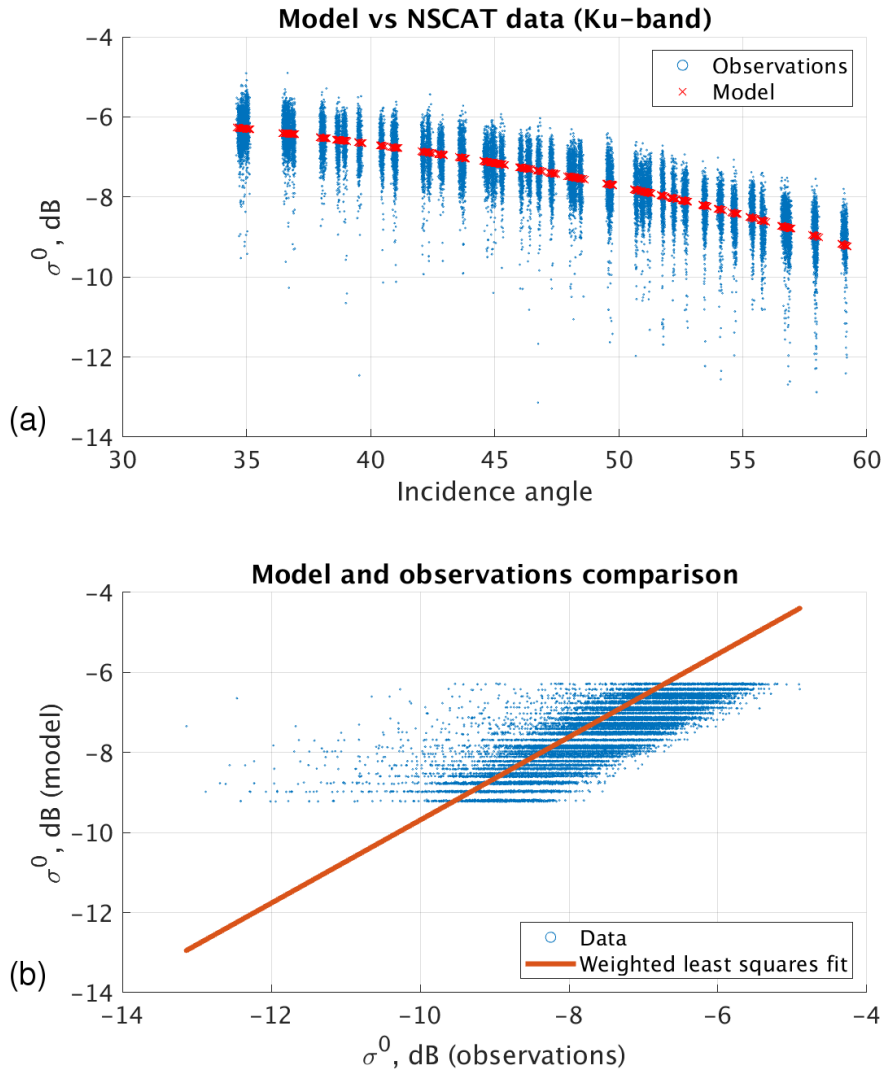

Figure 3.4: (a) The least squares fit of the volume scattering model in Eq. 3.19 to Ku-band NSCAT data over the Amazon rainforest. (b) The correlation between the volume scattering model to the NSCAT observations. The correlation coefficient between the data and the model is 0.8927 for 58147 NSCAT measurements. The estimated albedo $\hat{a}$ of the model is 0.7493. The NSCAT data is obtained from V-pol antenna beams 1, 2, and 4 from Julian day 1-30 of 1997.

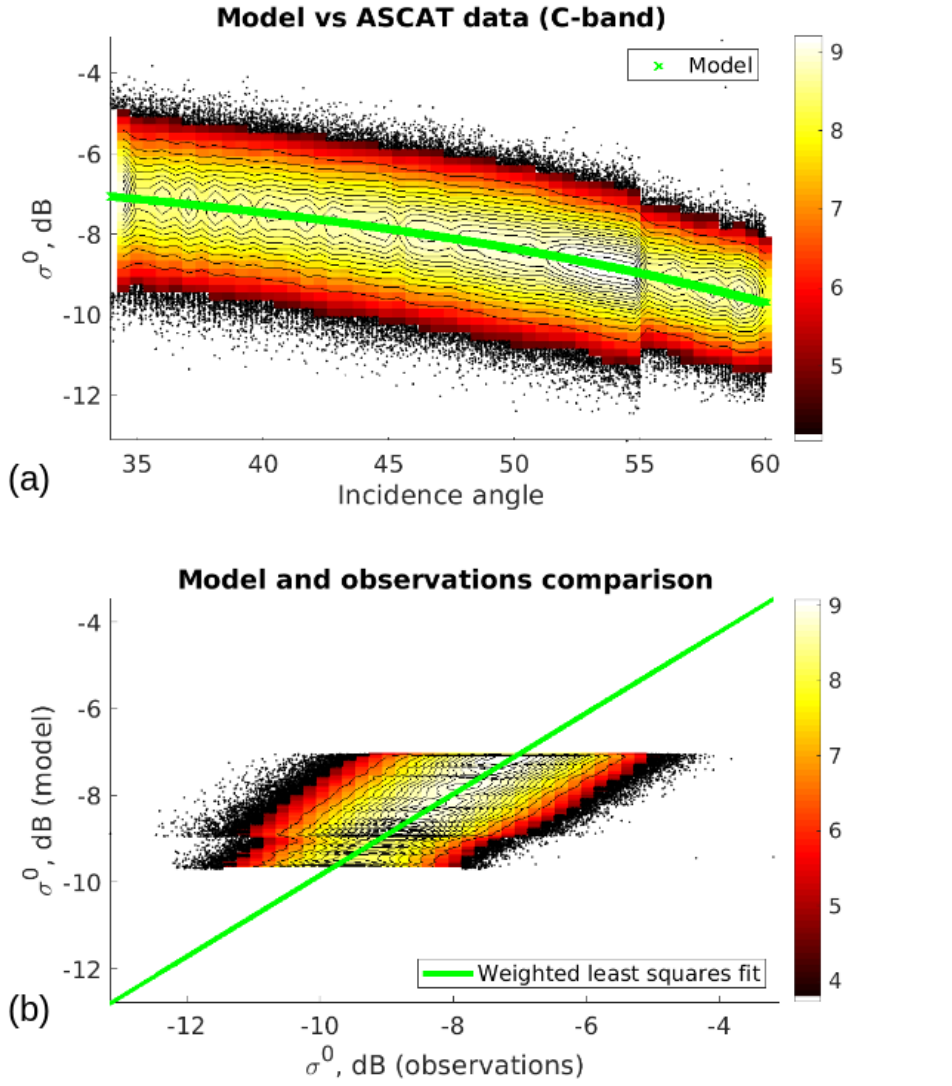

Figure 3.5: (a) The least squares fit of the volume scattering model in Eq. 3.19 to V-pol C-band ASCAT data over the Amazon rainforest. Due to the large number of ASCAT measurements used, a density plot is shown, where the units of the color bar are arbitrary and denote a higher density of measurements. (b) The correlation between the volume scattering model to the ASCAT observations. The correlation coefficient between the data and the model is 0.6914. The estimated albedo $\hat{a}$ is 0.5074. The ASCAT data is obtained from the fore, mid, and aft antennas of the right swath from Julian day 1-30 of 2007.

3.3 Results

A comparison of measured σ^0 to model-fit values using Eq. 3.21 is shown in Figs. 3.4 and 3.5 for Amazon observations $\mathbf{x}$ from NSCAT and ASCAT data, respectively. The correlation coefficient between the fit or estimate $\hat{\mathbf{x}}$ to the observations $\mathbf{x}$ is higher for the NSCAT fit than the ASCAT fit (0.8927 versus 0.6914). The assumed value for κ_e does not effect the least squares fit to the data. Any value for κ_e yields an estimated albedo of 0.7493 and 0.5469 for the fits to NSCAT and ASCAT data, respectively.

Since Eq. 3.21 is a function of incidence angle, it can be used to model the incidence angle dependence of σ^0. This model is compared to existing models for the incidence angle dependence of σ^0 in the following section.

3.4 Summary

A volume scattering model for σ^0 observed by scatterometers over the Amazon rainforest has been developed. This model fits reasonably well to ASCAT and NSCAT data where the correlation coefficient of the model to the data is 0.6914 and 0.8927 for ASCAT and NSCAT, respectively. The estimate for the albedo is an unbiased estimator based on the use of the SVD psuedoinverse to solve the matrix equation in Eq. 3.21.

CHAPTER 4. SCATTEROMETER CROSS CALIBRATION MODEL

In the previous chapter, a volume scattering model for σ^0 observed by scatterometers over the Amazon rainforest is developed. This model is now applied to model the incidence angle, frequency, and polarization dependence of σ^0.

To begin, σ^0 is modeled as the true signal with calibration biases plus noise,

$$\sigma^0_{meas}(\theta,\phi,F,pol,t) = \sigma^0_{true}(\theta,\phi,F,pol,t) + C + \eta, \tag{4.1}$$

where σ^0_{meas} and σ^0_{true} vary with incidence angle (θ), azimuth angle (ϕ), time (t), frequency (F, GHz) and polarization (pol). Although more parameters may be considered that cause σ^0_{meas} and σ^0_{true} to vary, this list is sufficient for this study. Since we are calibrating over a surface that is azimuthally isotropic, azimuth angle dependence is neglected. Since we are only considering measurements of similar polarization, polarization is ignored. Although ASCAT and NSCAT are temporally disjoint, averaging σ^0 measurements over a similar season of the year and time of day minimizes the time dependence and allows us to compare temporally disjoint data. We consider the noise η to be independent white Gaussian noise with zero mean, so averaging measurements over multiple days reduces the effects of noise to become negligible.

Removing unused terms, Eq. 4.1 becomes

$$\sigma^0_{meas}(\theta,F) = \sigma^0_{true}(\theta,F) + C, \tag{4.2}$$

where frequency and incidence are now the only parameters of interest.

Although $\sigma^0_{true}(\theta,F)$ may also vary for different surfaces and locations, we assume that there exists a deterministic $\sigma^0_{true}(\theta,F)$ which is independent of surface and location within the masked rainforest region. The goal of this section is to determine a calibration estimate for $\sigma^0_{true}(\theta,F)$ that is suitable for cross-calibration purposes within the Amazon mask.

We rewrite Eq. 4.2 using estimated parameters and known terms

$$\hat{\sigma}^0_{cal}(\theta,F) = \sigma^0_{meas}(\theta,F) + \hat{C}, \tag{4.3}$$

where $\hat{\sigma}^0_{cal}(\theta,F)$ is a calibration estimate for $\sigma^0_{true}(\theta,F)$ and $\hat{C}$ is an estimate for C.

We first discuss the incidence angle dependence, then explore the frequency dependence of σ^0 and a method to correct both simultaneously.

4.1 Incidence Angle Dependence Models

Several models exist for the incidence angle dependence of σ^0 over land calibration regions (typically the Amazon rainforest) observed from scatterometers. One such model is a first order polynomial fit to empirical data using least squares estimation as in [8, 10], or

$$\sigma^0_{cor}(F) = \sigma^0_{meas}(\theta,F) + B(\theta_{nom} - \theta), \tag{4.4}$$

where B denotes the dB/degree incidence angle dependence obtained from linear regression between θ and $\sigma^0_{meas}(\theta,F)$, θ_{nom} is the nominal incidence angle calibrated to, and θ is the incidence angle of $\sigma^0_{meas}(\theta,F)$. The resulting σ^0_{cor} represents $\sigma^0_{meas}(\theta,F)$ as a function of only one incidence angle θ_{nom} instead of the range of incidence angles in θ. A drawback of this model is that it is not based on the physics of backscatter for the Amazon rainforest; it is simply a first order solution.

Another incidence angle dependence model used for calibration using land targets is $\gamma^0(\theta)$ [27–29], where

$$\gamma^0(\theta,F) = \frac{\sigma^0_{meas}(\theta,F)}{cos(\theta)}. \tag{4.5}$$

One benefit of γ^0 is that it normalizes σ^0 by $\cos(\theta)$. This $\cos(\theta)$ dependence typically only occurs for the roughest of surfaces [2]. For volume scattering from the Amazon rainforest, the incidence angle dependence is $\frac{a}{2}cos(\theta)$, so γ^0 removes the incidence angle dependence. However, since γ^0 does not account for the albedo or an offset due to calibration, it is not useful for cross calibration purposes. The albedo contains the frequency dependence of σ^0, so γ^0 can only be used to normalize the incidence angle dependence at distinct frequencies. In addition, by not including

an offset due to calibration as in Eq. 4.2, γ^0 cannot be used to estimate cross calibration differences between sensors. It is also shown that γ^0 results in the highest variance in dB between the models.

To address the drawbacks of Eq. 4.4 and 4.5, Eq. 3.21 is used to correct the incidence angle dependence of σ^0 for land calibration targets. Eq. 3.21 is centered around the mean σ^0 for a wide range of incidence angles in both NSCAT and ASCAT, and the correction is

$$\sigma^0_{cor}(F) = \sigma^0_{meas}(\theta, F) + \mu_{\sigma^0}(F) - \sigma^0_{model}, \tag{4.6}$$

where μ_{σ^0} is the mean of $\sigma^0_{meas}(\theta)$, and σ^0_{model} is the modeled σ^0 from Eq. 3.21.

An example of the three incidence angle dependence models for σ^0 is given in Figs. 4.1 and 4.2. In both Figures, (a) is Eq. 4.4, (b) is Eq. 4.5, and (c) is Eq. 4.6. In (a), $\sigma^0_{cor}(F)$ is almost as consistent along the entire incidence angle range as (c). The variance is 0.178 dB for NSCAT and 0.541 dB for ASCAT. In (b), $\gamma^0(\theta, F)$ is a function of incidence angle for both NSCAT and ASCAT. The variance of $\gamma^0(\theta, F)$ is 0.2245 dB for NSCAT and 0.5457 dB for ASCAT. In (c), it is clear that σ^0_{cor} has less variation with respect to incidence angle as (b). The variance of $\sigma^0_{cor}(F)$ in (c) is the lowest for all three models as 0.168 dB for NSCAT and 0.534 dB for ASCAT.

Both Eqs. 4.4 and 4.5 have been used to demonstrate the stability of backscatter measurements for scatterometers for land calibration regions, and Eq. 4.4 has been used in cross calibration between multiple scatterometers. Since Eq. 3.21 has the lowest variance with respect to incidence angle of the three models and is physics based, we suggest this model as the most suitable of the three for scatterometer cross calibration and validation.

4.2 Frequency Dependence Model

According to Ulaby and Long, some of the most important considerations in developing a volume scattering model are the shape of the scatterers and the size distribution of the scatterers relative to the wavelength [15]. In developing a frequency dependence model for the volume scattering of the Amazon rainforest, both of these are considered. First, a scattering model for circular disks developed by Fung et al. [31] is used to approximate the volume backscattering coefficient of individual leaves in the Amazon rainforest. Second, a PDF of leaf radii is adopted from the histogram of leaf areas provided by Malhado et al. [23]. It is shown that since the Ku-

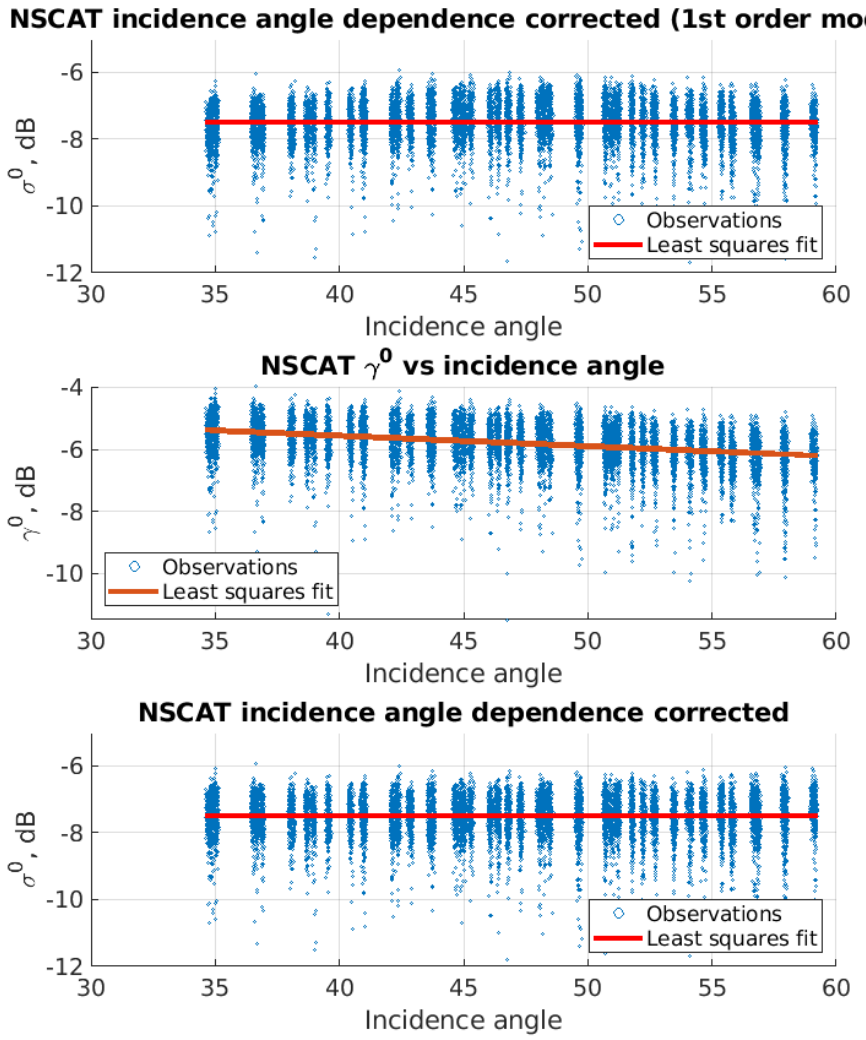

Figure 4.1: All three models for the incidence angle dependence of σ^0 for NSCAT data. As in Fig. 3.4 the data is obtained from Julian day 1-30 of 1997. Plot (a) is the result of Eq. 4.4 and has slightly higher variance than (c) of 0.178 dB. The negligible slope of the curve is -5.47e-14 dB/degree and the mean is -8.23 dB. Plot (b) is the result of Eq. 4.5 and has the highest variance of 0.2245 dB. The slope of the curve is -0.0338 dB/degree and the mean is -4.1882 dB. Plot (c) is the result of Eq. 4.6 and has the lowest variance in $\sigma^0_{cor}(F)$ for the incidence angle range of 0.168 dB. The slope of the curve is -1.8595e-5 dB/degree and the mean is -7..4799 dB.

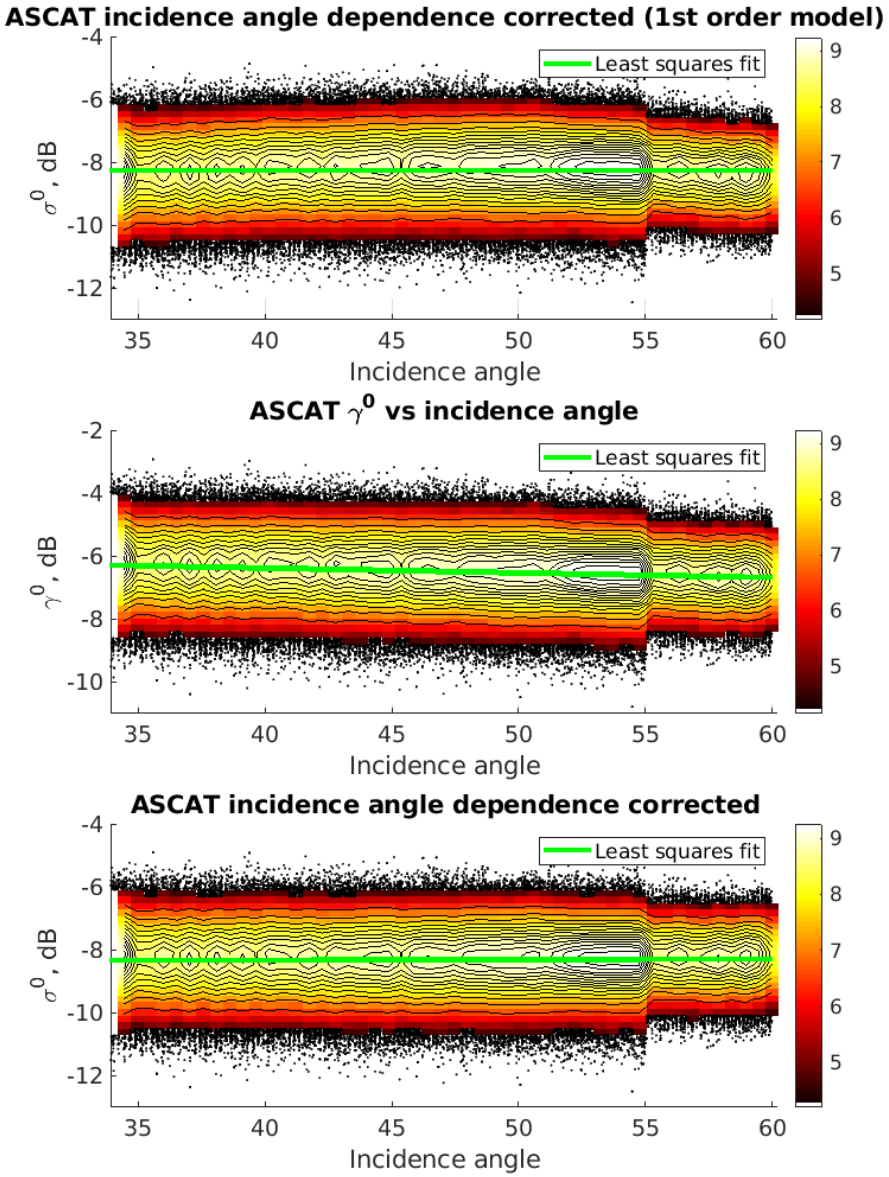

Figure 4.2: All three models for the incidence angle dependence of σ^0 for ASCAT data. As in Fig. 3.5 the data is obtained from Julian day 1-30 of 2007. Plot (a) is the result of Eq. 4.4 and has slightly higher variance than (c) of 0.541 dB. The negligible slope of the curve is -5.47e-15 dB/degree and the mean is -8.2344 dB. Plot (b) is the result of Eq. 4.5 and has the highest variance of 0.5457 dB. The slope of the curve is -0.0151 dB/degree and the mean is -5.7549 dB. Plot (c) is the result of Eq. 4.6 and has the lowest variance in $\sigma^0_{cor}(F)$ for the incidence angle range of 0.534 dB. The slope of the curve is 0.001 dB/degree and the mean is -8.3434 dB.

band wavelength of 2.14 cm is very close to the average leaf radius in the Amazon rainforest, which is approximately a delta function in the leaf radius PDF, a frequency dependence model is not feasible for Ku-band.

A model for scattering of a leaf estimated as a circular disk by Fung is used to model $\hat{\kappa}_e$ for leaves in the Amazon rainforest [31]. Since individual scatterers are observed in this model, the isotropic scattering assumption [15] for the Amazon rainforest canopy layer cannot be used. Instead, Eq. 2.3 is used, where $\sigma_v^{back}(F)$ is substituted for $\kappa_s(F)$ as

$$\sigma^0_{model}(\theta,F) = \frac{\sigma_v^{back}(F)}{\kappa_e(F)}\frac{cos(\theta)}{2} + C_f, \tag{4.7}$$

where $\sigma_v^{back}(F)$ is the volume backscattering coefficient as a function of frequency, $\kappa_e(F)$ is the extinction coefficient as a function of frequency, and C_f is the calibration offset due to frequency. The logarithmic and power law models for κ_e from Currie et al. [21] are used in this frequency dependence model.

4.2.1 Leaf Scattering Model

This subsection briefly describes the background for the equations for the backscattering cross section of the circular disk model from Fung [31].

The demagnetizing factors for a circular disk [33] are

$$g_T = \frac{1}{2(m^2-1)}\left(\frac{m^2}{\sqrt{m^2-1}}sin^{-1}\left(\frac{\sqrt{m^2-1}}{m}\right) - 1\right) \tag{4.8}$$

$$g_N = \frac{m^2}{m^2-1}\left(1 - \frac{1}{\sqrt{m^2-1}}sin^{-1}\left(\frac{\sqrt{m^2-1}}{m}\right)\right), \tag{4.9}$$

where $m = \frac{r}{h}$ and r is the radius and h is the half of thickness. The polarizability tensor [34] is

$$\mathbf{a} = a_T\mathbf{I} + (a_N - a_T)\hat{z}, \tag{4.10}$$

with

$$a_T = \frac{1}{(\varepsilon-1)g_T + 1} \tag{4.11}$$

$$a_N = \frac{1}{(\varepsilon - 1)g_N + 1} \tag{4.12}$$

and ε is the dielectric constant of the leaf. If the thickness is much smaller than the wavelength, and if $kt(\varepsilon)^{\frac{1}{2}} << 1$, where k is the wavenumber in meters and t is the thickness in meters, we can assume the generalized Rayleigh-Gans (GRG) approximation. With this approximation, the modifying function for a circular disk [35] is

$$\mu = 2\frac{J_1(Q_{si}r)}{Q_{si}r}, \tag{4.13}$$

where $J_1()$ is the cylindrical Bessel function of the first kind, and Q_{si} is

$$Q_{si} = 2ksin(\theta), \tag{4.14}$$

where θ is the incidence angle. The incidence angle is defined as the angle between the incident beam and the normal to the circular disk. The V-pol scattering amplitude in the backscattering direction is

$$F_V(-\hat{i},\hat{i}) = \frac{k^2(\varepsilon - 1)v_0}{4\pi}\left(a_N sin^2(\theta) + a_T cos^2(\theta)\right)\mu, \tag{4.15}$$

where v_0 is the volume of the scatterer and $(-\hat{i},\hat{i})$ denotes the backscattering direction. For H-pol,

$$F_H(-\hat{i},\hat{i}) = -\frac{k^2(\varepsilon - 1)v_0}{4\pi}a_T\mu. \tag{4.16}$$

The P polarized backscattering cross section is

$$\sigma_P = 4\pi \mid F_P(-\hat{i},\hat{i}) \mid^2. \tag{4.17}$$

The P polarized volume backscattering coefficient σ_P^{back}

$$\sigma_P^{back} = N_v \mid F_P(-\hat{i},\hat{i}) \mid^2, \tag{4.18}$$

where N_v is the number density. The number density accounts for the number of leaves for 1 cubic meter volume. For leaves in the Amazon rainforest, N_v is estimated as the number of leaves in ppm from Calvet et al. [36] multiplied by a and divided by the expected value of the leaf area.

Eq. 4.18 assumes a uniform distribution of leaf radii, where the leaf radii are accounted for in calculating the demagnetizing factors are well as the modifying function for a circular disk. To account for a non-uniform distribution of leaf radii, we re-write Eq. 4.18 as

$$\sigma_P^{back} = N_v \mid \sum_r \rho F_P(-\hat{i},\hat{i},r) \mid^2, \tag{4.19}$$

where the summation is over the distribution of the leaf radii, ρ is the PDF of the leaf radii, and $F_P(-\hat{i},\hat{i},r)$ is a function of the leaf radii. In calculating the volume backscattering coefficient, several thousand realizations of leaf radii are simulated, and the resulting forward scattering amplitudes in the backscattering direction are averaged together.

The extinction coefficient is the same model by Currie et al. [21] introduced in Chapter 3, where

$$\kappa_e = a + b\left(log_{10}(F)\right), \tag{4.20}$$

where $a = 1.102$ and $b = 1.48$, and

$$\kappa_e = sF^{\frac{3}{4}}, \tag{4.21}$$

where $s = 0.25$.

To examine only the frequency dependence of σ^0, the $cos(\theta)/2$ term in Eq.4.7 is removed such that

$$\sigma^0_{model}(F) = \frac{\sigma_P^{back}(F)}{\kappa_e} + C_f, \tag{4.22}$$

where only the frequency dependent terms are included in the model.

4.2.2 Leaf Scattering Model Parameters

As seen in the derivation of the leaf scattering model, there are several parameters that the model is dependent on. These parameters include the leaf radius r, thickness t, dielectric constant ε, wavelength λ, incidence angle θ. All of these parameters are described in greater detail in this subsection. The leaf radius is an essential parameter for the leaf scattering model applied to the

Amazon rainforest. To properly model the response of an average leaf in the Amazon rainforest, the expected value of the leaf radius is needed. To calculate the expected value, a PDF of the leaf radii is needed.

A PDF of leaf radii in the Amazon rainforest is estimated as the histogram or reported leaf sizes given in Malhado et al. [23]. Although probably not realistic, the leaf radius values from Malhado et al. are assumed to be uniformly distributed within each bin width. A PDF could be estimated by fitting a distribution to the data, such as a Rayleigh distribution; however, since the leaf radii are distributed as approximately a delta function at a leaf radius of 2.6 cm, such a distribution would not fit well to the histogram.

The bin widths used by Malhado et al. are quite uneven, and this leads to an abnormally distributed histogram. The original histogram with 7 bins is seen in Fig. 4.3. The 7 bins have uneven bin widths, these bin edges are: 0-0.28 cm, 0.28-0.85 cm, 0.85-2.54 cm, 2.54-2.76 cm, 2.76-7.62 cm, 7.62-22.85 cm, and 22.85-24.2 cm. An equivalent histogram with 100 even bin edges is given in in Fig. 4.4. The leaf radii are distributed into many bins below 6 centimeters, but very large bin widths are used for leaf radii above 6 centimeters, causing a very abnormal distribution. The even-binned histogram shows a very large spike in probability for one bin at approximately 2.6 cm. It is shown that this spike results in resonant behavior in the frequency dependence at 2.6 cm, which is very close to the NSCAT wavelength of 2.14 cm. This causes the frequency dependence of σ^0 to be very sensitive to the precise leaf radius model in Ku-band.

A Rayleigh PDF is fit to the histogram using even bin widths given in Fig. 4.4. The Rayleigh PDF is fit to the histogram using the maximum likelihood estimator of the Rayleigh parameter as

$$B = \frac{1}{2n}\sum_{i=1}^{n} x_i^2, \tag{4.23}$$

where n is the number of realizations, and x_i is the leaf radius. It is shown in Fig. 4.5 that neither PDF is a good estimate of the histogram, so the histogram is used as the PDF to calculate the expected value of the leaf radius of the Amazon rainforest. This expected value is used as the radius for the leaf scattering model.

Several other parameters are much easier to compute. The leaf thickness t is used from a report by Calvet et al. for estimates of soil moisture in the Amazon rainforest as 0.4 mm [36].

The wavelength λ is chosen to be wavelengths between the NSCAT Ku-band wavelength of 2.14 and the ASCAT C-band wavelength of 5.71 cm. The incidence angle θ is given by the range of incidence angle observed by ASCAT and NSCAT. The dielectric constant is estimated using a dielectric model for vegetation by El-Rayes and Ulaby given in [15]. This model uses empirical fits to dielectric measurements of vegetation from 0.2 to 20 GHz and is dependent on two parameters, the gravimetric moisture content *mg* and the frequency in GHz F. The gravimetric moisture content describes the moisture content of a vegetation material, such as a leaf. The value for *mg* is also taken from Calvet et al. as 0.83 g/cm^3 [36].

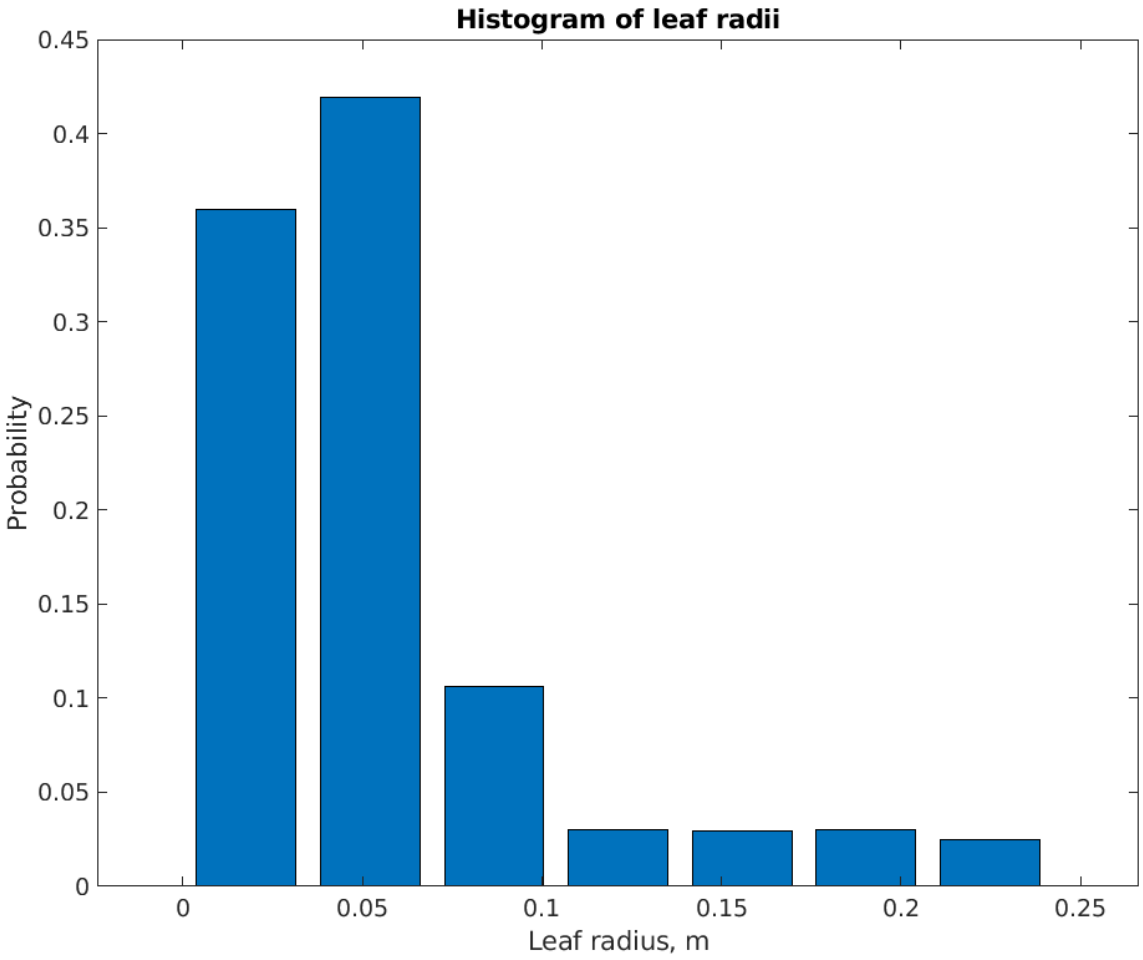

Figure 4.3: The histogram of leaf radii with 7 bins provided by [23].

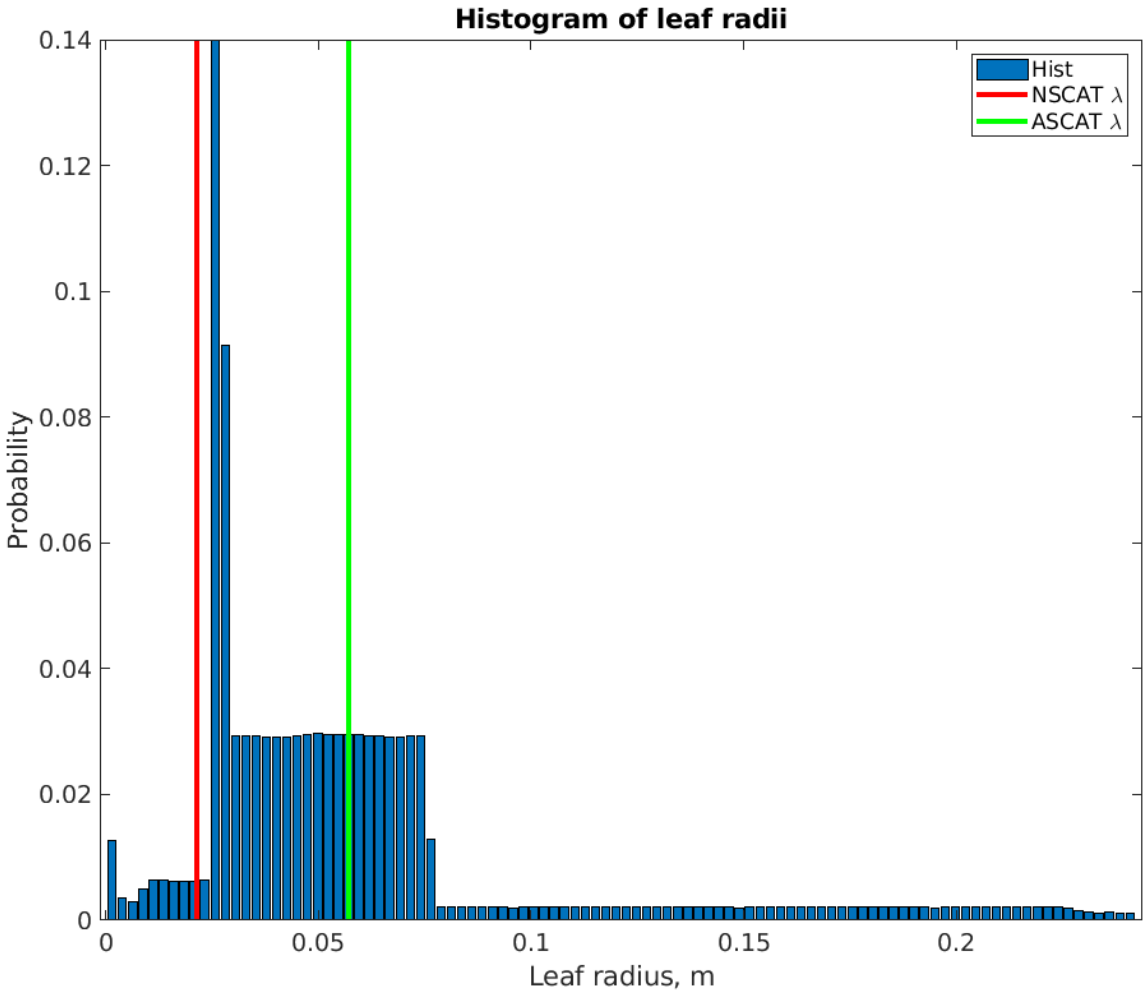

Figure 4.4: A histogram of the realized leaf radii based on the histogram provided by Malhado et al. [23]. 3000 realizations of the length 2000 leaf radius random variable vectors were averaged together to create a mean leaf radius vector for the histogram. The NSCAT and ASCAT wavelengths are as colorized lines for reference, where it is observed that the NSCAT wavelength of 2.14 cm is very close to the peak of the histogram at approximately 2.6 cm.

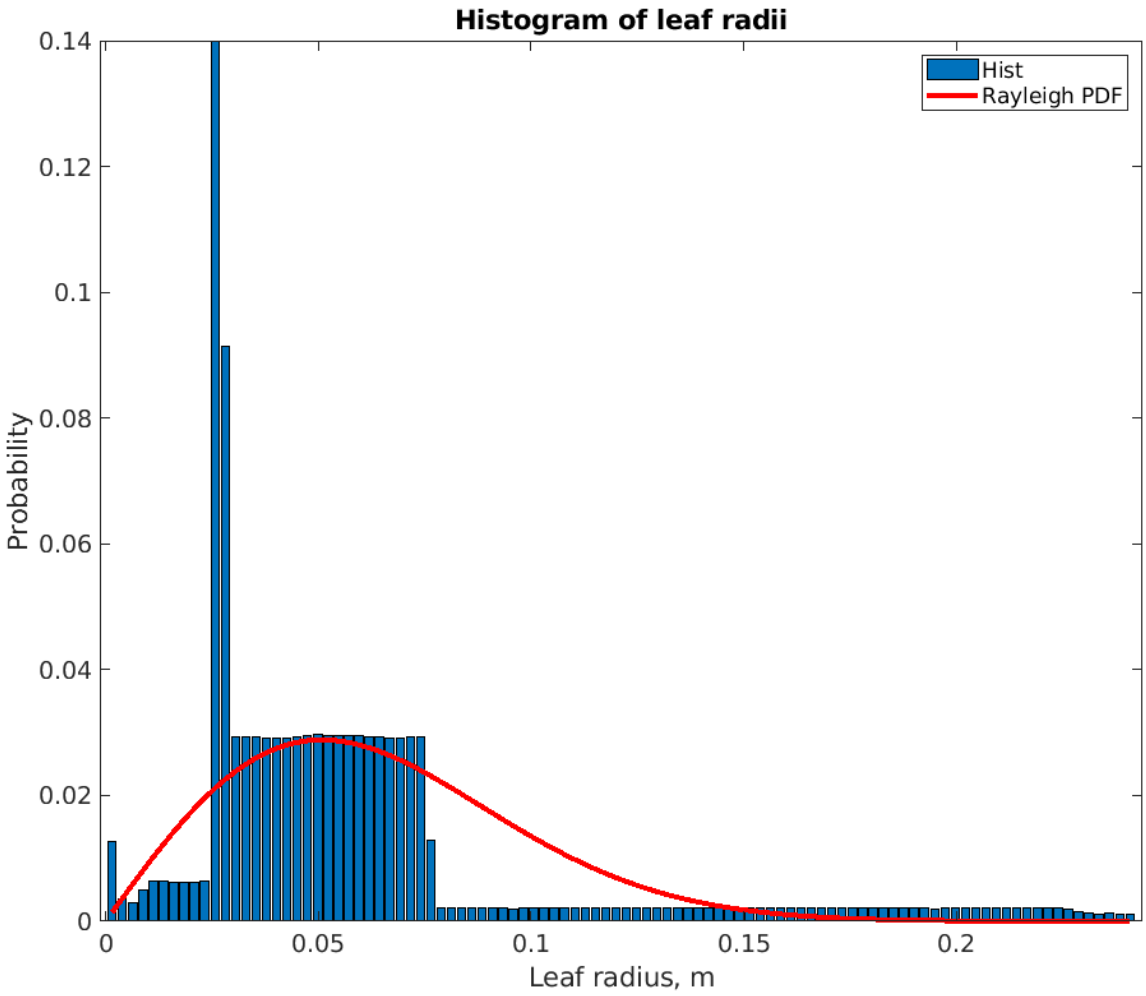

Figure 4.5: The fit of a Rayleigh PDF to the histogram of the leaf radii based on the histogram provided by Malhado et al. [23]. The same histogram as in Fig. 4.4 is used and a Rayleigh PDF is fit to the histogram using the maximum likelihood estimator of the Rayleigh parameter in Eq. 4.23. The Rayleigh PDF smooths out the disjoint bin heights of the histogram, however, it does not capture the peak probability at 2.6 cm. Since the histogram is abnormally distributed and a Rayleigh PDF is not a good fit, the histogram is used as the PDF for calculating the expected value of the leaf radius.

The σ^0 frequency dependence from C-band to Ku-band is shown in Fig. 4.6. 3000 realizations of length 2000 vectors of the forward scattering amplitude are averaged together with their respective length 2000 leaf radius random variable vectors. We note that there is a dip in the frequency dependence of σ^0 at 12 GHz which corresponds to the 2.6 cm leaf radius which dominates the PDF. Since this dip is so close to the NSCAT frequency at 13.995 GHz, it may not be not feasible to use this leaf scattering model to model the Ku-band frequency dependence of σ^0. However, this sensitivity may help explain why NSCAT σ^0 is approximately 1 dB high than other Ku-band scatterometers at similar polarizations and incidence angles as observed by Madsen et al. [13]. NSCAT operates at 13.995 GHz, which is approximately 1 dB higher than 13.4 GHz for the V-pol σ^0 frequency model in Fig. 4.6. It is not suggested to cross calibrate from Ku-band to C-band due to the dip at 12 GHz.

The dip at 12 GHz suggests that σ^0 is highly sensitive to the leaf radius of the Amazon rainforest. In Appendix A, a spatial gradient of σ^0 of the Amazon rainforest is observed. This spatial gradient is created with QSCAT SIR images from the year 2009. The spatial gradient correlates very well with a leaf size gradient observed by Malhado et al. [23]. We suggest that in order to develop the σ^0 frequency dependence, more knowledge of the leaf radii of the Amazon rainforest is needed. More field data would help create a true PDF of the leaf radii, and field data in many areas over the spatial gradient in σ^0 may correlate well with larger and smaller leaf sizes.

4.3 Polarization Dependence

For the incidence angle and frequency dependence models, only V-pol σ^0 are considered since ASCAT only has V-pol σ^0 measurements. NSCAT has both horizontal and V-pol σ^0, and the calibration difference between the two has been measured as about a 1.5 dB difference [13]. Utilizing the horizontal and V-pol forward scattering amplitudes, the polarization dependence for a leaf in the Amazon rainforest canopy can be observed.

The leaf scattering model for the forward scattering amplitude in both polarizations is in linear units, not dB. Therefore, a ratio of the horizontal and V-pol σ^P_{model} in Eq. 4.22 describes the dependence between the polarizations.

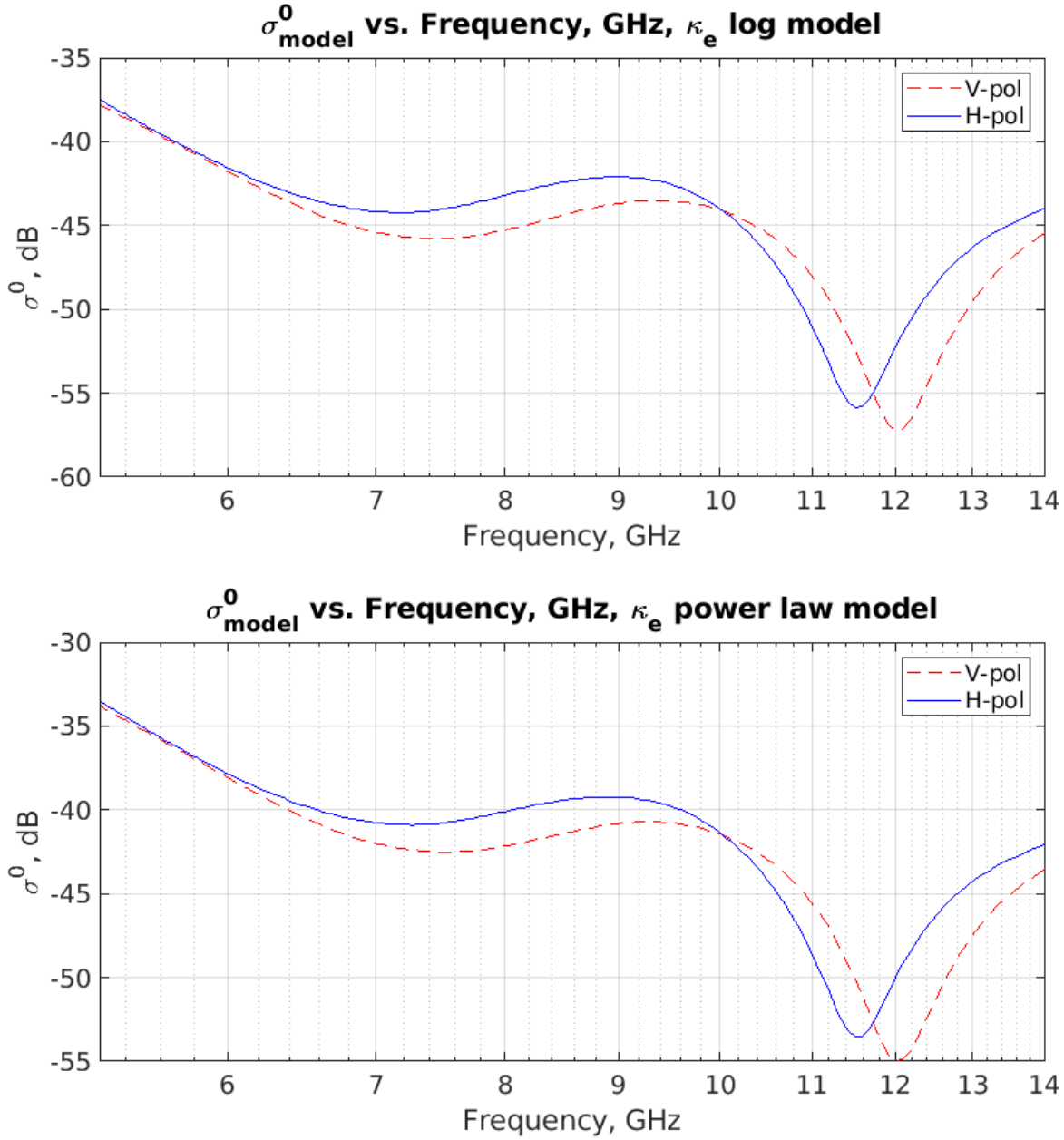

Figure 4.6: The σ^0 frequency dependence model using both κ_e models from Currie et al. [21]. The forward scattering amplitude, which is used to calculate the volume backscattering coefficient, is averaged together for 3000 realizations of length 2000 leaf radius random variable vectors.

Since both models for κ_e are polarization independent [21], Eq. 4.22 reduces to

$$\sigma_{ratio}^{H/V} = \frac{\mid F_H(-\hat{i},\hat{i}) \mid^2}{\mid F_V(-\hat{i},\hat{i}) \mid^2}. \tag{4.24}$$

Combining Eq. 4.24 with the calibration equation Eq. 4.2,

$$\sigma_{meas}^{H} - \sigma_{meas}^{V} = \sigma_{ratio}^{H/V} + C_{pol}, \tag{4.25}$$

where σ_{meas}^{H} is the measured H-pol σ^0, σ_{meas}^{V} is the measured V-pol σ^0, and C_{pol} is the calibration offset between the measured σ^0 ratio and the modeled σ^0 ratio.

Although there are no H-pol C-band scatterometers to verify the polarization ratio, several dual polarized Ku-band scatterometers exist. As observed by Madsen et al. [13], the polarization ratio between H- and V-pol σ^0 in Ku-band is approximately 1.5 dB. In Fig. 4.7, the polarization ratio is 1.618 at 14 GHz. Therefore, $C_{pol} = 0.118$ dB for NSCAT observations.

4.4 Summary

An incidence angle dependence model based on the volume scattering model for the Amazon rainforest has been shown to normalize the incidence angle dependence of σ^0. This is an advantage over the γ^0 model since the γ^0 normalization is only applicable to very rough surfaces. The normalization of the new model is also an advantage over the first order model since the first order model can only normalize σ^0 to a single incidence angle. In addition, the new incidence angle dependence model has lower variance than previous models, and is based on the volume scattering physics for the calibration regions, unlike the other two models.

The frequency dependence of σ^0 for leaves in the Amazon rainforest has been described. Due to the field data used to create the distribution of the leaf radii, a dip has been discovered in the frequency dependence of σ^0 at 12 GHz, which is very close to Ku-band. This dip causes the frequency dependence of σ^0 to be very sensitive. Without better knowledge of the leaf size distribution, using the model for scattering from leaves to describe the frequency dependence of σ^0 is not sufficient for a cross calibration model for σ^0 between C- and Ku-band. Since Ku-band is very close to the dip at 12 GHz, it is also not suggested to use this model to cross calibrate

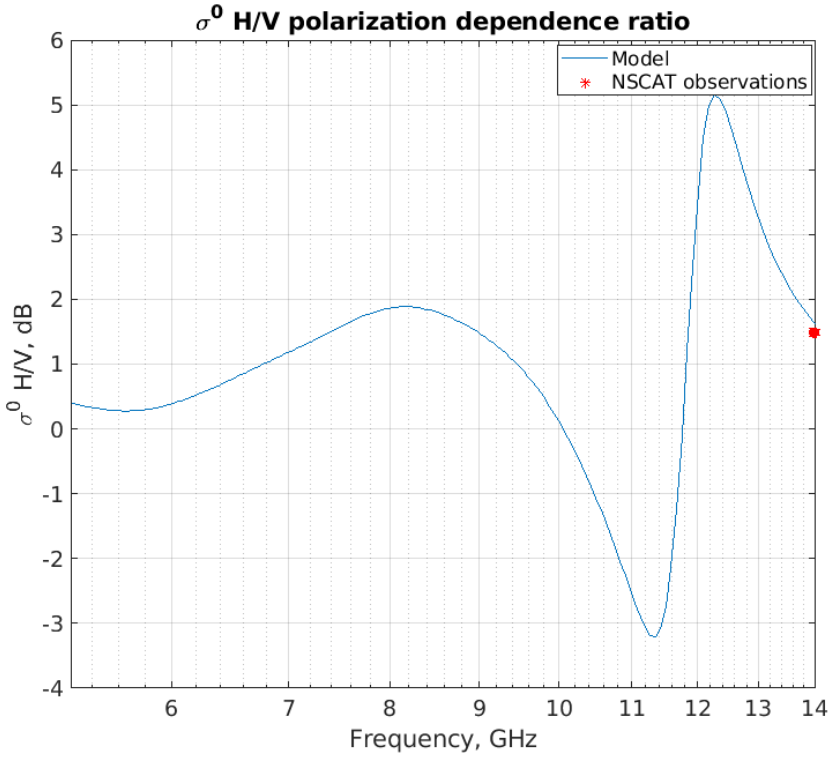

Figure 4.7: Ratio of H- and V-pol σ^0 from C-band to Ku-band. Although there are no dual polarized C-band scatterometers to verify the polarization ratio, NSCAT H- and V-pol σ^0 agree well with this ratio.

between Ku-band σ^0. However, the sensitivity of σ^0 in this frequency band over the Amazon rainforest due to the dip may explain why NSCAT is approximately 1 dB higher than other Ku-band scatterometers whose operating frequencies are approximately 500 MHz below it, such as QSCAT.

A model for the polarization dependence of σ^0 between H- and V-pol has been introduced. This model is based on the frequency dependence model from the scattering of leaves in the Amazon rainforest. Although there are no C-band dual polarized scatterometers that offer H-pol σ^0, several Ku-band scatterometers are dual polarized. It is shown that the polarization dependence model agrees well with observed differences in H- and V-pol σ^0 at Ku-band by Madsen et al. [13], where the difference between the model and observations is approximately 0.118 dB.

CHAPTER 5. CONCLUSION

5.1 Summary

This thesis develops and analyzes a volume scattering model for use in calibration of σ^0 between scatterometers of different frequencies and incidence angles over volume scattering regions.

Chapter 1 introduces scatterometers and provides a road-map for this thesis. It contains the thesis statement and motivation to prepare for the subsequent chapters.

Chapter 2 provides essential background for understanding the technical content in Chapters 3 and 4. It provides background on the ASCAT, NSCAT, and QSCAT scatterometers whose data are used in this thesis. In addition, it provides the background for the Amazon rainforest as a volume scattering calibration region.

Chapter 3 develops the volume scattering model used in Chapter 4. It derives the model based on a simple EM volume scattering model for use in cultural vegetation canopies. It also addresses how well the model fits to observed data from NSCAT and ASCAT.

Chapter 4 develops several models for cross calibration of σ^0. There are several models for the incidence angle dependence of σ^0, however, none of them are based on backscatter physics. A physics based volume scattering model is derived and shown to have lower variance than current models in addition to normalizing the incidence angle dependence of σ^0 over volume scattering regions.

Chapter 4 also introduces a model for the frequency dependence of σ^0. A model for the frequency dependence of σ^0 is developed using a thin cylindrical disk scattering model adapted to leaves of the Amazon rainforest. Parameters for this scattering model stem from field data taken from the Amazon rainforest, such as leaf thickness, gravimetric moisture content, and leaf radii. A null is the frequency dependence has been discovered using field data for the distribution of the leaf radii. Since this null at 12 GHz is very close to Ku-band, Ku-band σ^0 is quite sensitive with

respect to frequency. Therefore, it is not suggested to use this model to cross calibrate σ^0 within Ku-band, or from C-band to Ku-band. Instead, more knowledge of the distribution of leaf sizes and field data are suggested to create a more sophisticated model. In addition, statistics of other biomass, such as branches, twigs, vines, and trunks, would also be beneficial in creating a more sophisticated model. A model based on leaf scattering alone is not sufficient for the frequency dependence of σ^0, but leads greater insight into the sensitivity of σ^0 with respect to frequency at Ku-band. The thin cylindrical disk scattering model is also shown useful in developing a model for the polarization dependence of σ^0. This polarization model agrees well with observed H- and V-pol Ku-band σ^0 from [13], where the difference between the modeled and observed σ^0 polarization ratio is approximately 0.118 dB.

5.2 Future Work

The volume scattering model provided in this thesis has many future applications in scatterometer calibration. An abbreviated list of future calibration applications follows:

5.2.1 Comparison to QSCAT σ^0

The incidence angle dependence model can be used to normalize the incidence angle dependence of fan beam scatterometers such as NSCAT and ASCAT. It can also be used to compensate for incidence angle variations between QSCAT slice measurements. Applying the incidence angle model to QSCAT σ^0 can normalize the incidence angle dependence at V- and H-pol σ^0 for cross calibration studies between NSCAT and QSCAT.

5.2.2 SIR A' and B' Images

The Scatterometer Image Reconstruction (SIR) algorithm for ASCAT and NSCAT currently creates A and B images based on the first order polynomial incidence angle dependence model. The new incidence angle dependence model can be used to create albedo (B') images as well as σ^0 images (A') that have had the incidence angle dependence normalized. Preliminary work in this area has shown that the new incidence angle dependence model correctly removes

the ‘rainbow’ effect of the incidence angle in A’ images and creates and albedo B’ image that reflects an albedo similar to the the estimated albedo in Ch. 3 for ASCAT across the entire Amazon rainforest region.

5.2.3 Frequency Dependence Models for Cross Calibration

This thesis provides the ground work for a frequency dependence model of σ^0 for volume scattering regions. It is suggested that more field data be observed for leaf radii in the Amazon rainforest at various locations to provide more insight into the distribution of leaves. Since the Amazon rainforest is not perfectly homogeneous, the field data from a distinct region is not enough to create a model that reflects the entire region. In addition, with statistics on other biomass that contribute to volume scattering, a more sophisticated model can be created that accurately reflects the volume scattering of the Amazon rainforest. The model in this thesis only accounts for leaves which are the main volume scattering mechanism. However, branches, twigs, and other biomass also contribute as volume scatterers. Since a simple model based on leaves alone is not sufficient to accurately create a model for cross calibration of σ^0 from C-band to Ku-band, perhaps a more sophisticated model can be used.

REFERENCES

[1] F. Naderi, M. H. Freilich, and D. G. Long, "Spaceborne radar measurement of wind velocity over the ocean - An overview of the NSCAT scatterometer system," *Proc. IEEE*, vol. 79, pp. 850-866, June 1991. 1

[2] D. G. Long, "Polar applications of spaceborne scatterometers", *IEEE Transactions on Geoscience and Remote Sensing*, vol. 10, no. 5. pp. 2307-2320, May 2017. 1, 2, 3, 6, 11, 30

[3] T. Mai, 'Meteorological Operational Satellite A (MetOp-A)', 2014. [Online]. Available:https://www.nasa.gov/directorates/heo/scan/services/missions/earth/MetOpA.html. 7

[4] D. G. Long, 'NSCAT Ocean Wind Measurement', 2002. [Online]. Available:https://www.mers.byu.edu/NSCAT.html. 9

[5] D. G. Long and P. J. Hardin, "Vegetation studies of the amazon basin using enhanced resolution Seasat scatterometer data", *IEEE Transactions on Geoscience and Remote Sensing*, vol. 32, no. 2, pp. 449-460, March 1994. 1, 2, 11

[6] D. G. Long and G. B. Skouson, "Calibration for spaceborne scatterometers using tropical rain forests," *IEEE Transactions on Geoscience and Remote Sensing*, vol. 34, no. 2, pp. 413-424, Mar. 1996. 1, 3, 9, 11, 51

[7] J. N. Huddleston, W. Tsai, M. W. Spencer, B. W. Stiles, and R. S. Dunbar, "SeaWinds on QuikSCAT: Postlaunch calibration and validation," in *Proc. IEEE IGARSS*, 2000, vol. 3, pp. 1024-1026. 3, 11

[8] I. J. Birrer, E. M. Bracalente, G. J. Dome, J. Sweet, and G. Berthold, "σ^0 signature of the Amazon rainforest obtained from the Seasat scatterometer," *IEEE Transactions on Geoscience and Remote Sensing*, vol. GRS-20, no. 1, pp. 11-17, 1982. 3, 9, 11, 30, 51

[9] W. Tsai, J. E. Graf, C. Winn, J. N. Huddleston, R. S. Dunbar, M. H. Freilich, F. J. Wentz, D. G. Long, and W. L. Jones, "Postlaunch sensor verification and calibration of the NASA scatterometer," *IEEE Transactions on Geoscience and Remote Sensing*, Vol. 37, pp.1517-1542, May 1999. 3, 13

[10] L. B. Kunz and D. G. Long, "Calibrating SeaWinds and QuikSCAT scatterometers using natural land targets", *IEEE Geoscience and Remote Sensing Letters*, vol. 2, no. 2, pp. 182-186, 2005. 3, 10, 30

[11] N. C. Currie, E. E. Martin, and F. B. Dyer, "Radar foliage penetration measurements at millimeter wavelengths", Tech. Rep. No. 4, Engineering Experiment Station, Georgia Inst. Technol., 31 Dec., Contract DAAA 25-73-C-0256 (NTIS AD A023838), 1975. 16, 17

[12] J. Barrus, "Intercalibration of Quikscat and OSCAT land backscatter," Masters Thesis, Brigham Young University, Provo, UT, Dec. 2013. 9, 10, 11, 16, 22, 51

[13] N. Madsen, "Calibration and validation of the RapidSCAT scatterometer," Masters Thesis, Brigham Young University, Provo, UT, Sept. 2015. 9, 10, 11, 14, 41, 43, 44, 46, 51, 53

[14] Y. Wang, L. L. Hess, S. Filoso, and J. M. Melack. "Understanding the radar backscattering from flooded and nonflooded Amazonian forests: Results from canopy backscatter modeling". *Remote Sensing of Environment*, vol. 54, no. 3, pp.324-332, 1995. 11, 13, 15, 17, 22

[15] F. T. Ulaby and D. G. Long, *Microwave Radar and Radiometric Remote Sensing.* Ann Arbor: The University of Michigan Press, 2014. 11, 12, 13, 15, 22, 23, 31, 34, 38

[16] C. Swift, "SeaSat scatterometer observations of sea ice," *IGARSS97. 1997 IEEE International Geoscience and Remote Sensing Symposium Proceedings. Remote Sensing - A Scientific Vision for Sustainable Development,* Mar. 1999. 12, 22

[17] A. G. Konings, M. Piles, K. Rtzer, K. A. Mccoll, S. K. Chan, and D. Entekhabi, "Vegetation optical depth and scattering albedo retrieval using time series of dual-polarized L-band radiometer observations," *Remote Sensing of Environment,* vol. 172, pp. 178189, 2016. 15

[18] A. Nashashibi, F. T. Ulaby, P. Frantzis, and R. D. De Roo, "MMW measurements of the extinction and volume backscattering coefficients of tree canopies at near grazing incidence," report, The University of Michigan, Ann Arbor, MI. 15, 22

[19] E. H. Helmer and M. A. Lefsky. "Forest canopy heights in Amazon River basin forests as estimated with the geoscience laser altimeter system (GLAS)," USDA Forest Service Proceedings RMRS-P-42CD, 2006. 15, 16

[20] D. E. Pitts, G. D. Badhwar, and E. Reyna, "The use of a helicopter mounted ranging scatterometer for estimation of extinction and scattering properties of forest canopies Part II: Experimental results for high-density aspen," *IEEE Transactions on Geoscience and Remote Sensing*, vol. 26, no. 2, pp. 144-152, 1988. 16

[21] N. Currie, F. Dyer, and E. Martin, "Millimeter foliage penetration measurements," *1976 Antennas and Propagation Society International Symposium,* Oct. 1976. 17, 34, 36, 42, 43

[22] Y. Kuga, M. W. Whitt, K. C. Mcdonald, and F. T. Ulaby, Scattering models for distributed targets in *Radar Polarimetry for Geoscience Applications* (F.T. Ulaby and C. Elachi, Eds.), Artech House, Dedham, MA, pp.111-190, 1990. 17

[23] A. Malhado, Y. Malhi, R. Whittaker, R. Ladle, H. ter Steege, L. L. Aragão, C. Quesada, A. Araujo-Murakami, O. Phillips, J. Peacock, G. Lopez-Gonzalez, T. Baker, N. Butt, L. Anderson, L. Arroyo, S. Almeida, N. Higuchi, T. Killeen, A. Monteagudo, D. Neill, N. Pitman, A. Prieto, R. Salomão, N. Silva, R. Vásquez-Martínez, and W. Laurance, "Spatial trends in leaf size of Amazonian rainforest trees," *Biogeosciences Discussions*, vol. 6, no. 1, pp. 2125-2162, 2009. 11, 20, 21, 31, 37, 38, 39, 40, 41, 51, 54, 55

[24] F. T. Ulaby, R. K. Moore, and A. K. Fung, *Microwave Remote Sensing, vol. III.* Norwoord, MA: Artech House, 1986, ch. 21. 22

[25] T. Moon and W. Stirling, *Mathematical Methods and Algorithms for Signal Processing.* Upper Saddle River, New Jersey: Prentice Hall, 2000. 24

[26] L. Scharf and C. Demeure, *Statistical Signal Processing.* Reading [etc.]: Addison-Wesley publishing Company, 1991. 25

[27] P. L. Frison and E. Mougin, "Use of ERS-1 wind scatterometer data over land surfaces", *IEEE Transactions on Geoscience and Remote Sensing*, vol. 34, no. 2, pp. 550-560, Mar. 1996. 30

[28] R. Crapolicchio and P. Lecomte, "On the stability of Amazon rainforest backscattering during the ERS-2 scatterometer mission lifetime," in *Proc. Envisat/ERS Symp.*, Salzburg, Austria, Sep. 2004, pp. 1-8. 30

[29] C. Anderson, J. Figa, H. Bonekamp, J. J. W. Wilson, J. Verspeek, A. Stoffelen, M. Portabella, "Validation of backscatter measurements from the advanced scatterometer on MetOp-A", *Journal of Atmospheric and Oceanic Technology*, vol. 29, pp.77-88, Jan. 2011. 30

[30] S. A. Bhowmick, R. Kumar, and A. S. K. Kumar, "Cross calibration of the OceanSAT-2 scatterometer with QuikSCAT scatterometer using natural terrestrial targets," *IEEE Transactions on Geoscience and Remote Sensing*, vol. 52, no. 6, pp. 33933398, 2014. 13

[31] M. A. Karam, A. K. Fung, and Y. M. M. Antar, "Electromagnetic wave scattering from some vegetation samples," *IEEE Transactions on Geoscience and Remote Sensing*, vol. 26, no. 6, pp. 799-808, 1988. 31, 34

[32] A. K. Fung, *Microwave Scattering and Emission Models and Their Applications.* Norwoord, MA: Artech House, 1994.

[33] J. A. Osborn, "Demagnetizing factors of the general ellipsoid," *Phys. Rev.*, vol. 67, pp. 351-357, 1945. 34

[34] M. A. Karam, "Remote sensing of random media with electromagnetic wave: A discrete approach," PhD. dissertation, the University of Kansas, 1984. 34

[35] N. N. Lebedev, *Special Functions and Their Applications.* New York: 1972, pp. 124-126. 35

[36] J. C. Calvet, J. P. Wigneron, E. Mougin, Y. H. Kerr, and J. L. S. Brito, *Plant Water Content and Temperature of the Amazon Forest from Satellite MIcrowave Radiometry*, vol. 32, no. 2, pp.397-408, 1994. 36, 37, 38

APPENDIX A. SPATIAL GRADIENT OF THE AMAZON MASK

A.1 Introduction

The Amazon rainforest has been used as a calibration region for scatterometers extensively due to its desirable scattering properties [6, 8, 12, 13]. The Amazon rainforest is composed of a dense canopy layer that exhibits mainly volume scattering, is isotropic with respect to azimuth angle, and is homogeneous with respect to several parameters. It is seasonally invariant, and exhibits diurnal changes due to the dew drying on the leaves throughout the day [13].

To utilize the Amazon rainforest as a calibration region, areas that exhibit homogeneity with respect to σ^0 are binary masked as 1, while areas that don't exhibit similar homogeneity are binary flagged as 0. This masking method is described in Chapter 2.

Despite the desirable scattering qualities of a binary mask of the Amazon rainforest, there is a slight spatial gradient along the Amazon calibration mask. The Amazon as an entire region is not completely homogeneous, there are rivers and tributaries near the Amazon river, and various canopy structures such as Terra firme in the southwest region [23]. These variations along the region lead to a north-south spatial gradient of σ^0 along the region on the order of 1 dB. The areas of the spatial gradient where σ^0 has a positive bias correlated with areas where Malhado et al. have reported larger leaf sizes, while areas with a negative bias correlate with areas that have smaller reported leaf sizes [23].

This appendix illustrates the spatial gradient of σ^0 in the Amazon mask, as well as the temporal and spatial stability of QSCAT σ^0 for the region and sub-regions despite the gradient. In addition, an example of the azimuth modulation of the OSCAT-2 scatterometer is shown over the spatial gradient, and that the spatial gradient does not cause the azimuth modulation. This leads us to believe that this azimuth modulation is due to the disjoint pointing of the fore and aft azimuth looks of the pencil beam antenna of OSCAT-2.

A.2 Calibration Region

The Amazon rainforest mask is derived from all of the 4-day SIR images of QSCAT in the year 2009. Both H- and V-pol images are used, as well as ascending and descending pass images. As described in Chapter 2, pixels with a standard deviation of less that 0.5 dB and within 1 dB of the mean σ^0 are included in the mask. All pixels that do not fall under this criteria for the entire year are flagged as 0. An example of a QSCAT SIR image of the Amazon rainforest is given in Fig. A.1.

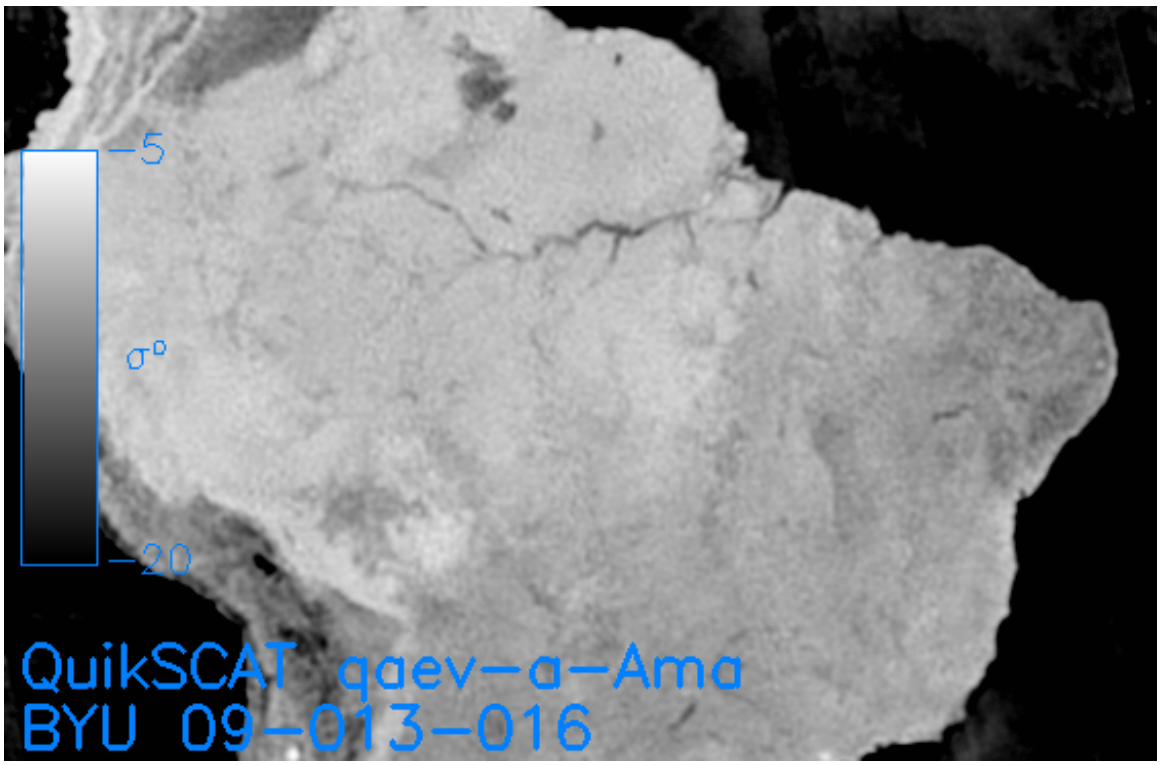

Figure A.1: A QSCAT V-pol SIR image of the Amazon rainforest region. 4 days of σ^0 data are used to create the image.

A.3 Spatial Bias

To demonstrate the spatial bias of the mask, σ^0 data from QSCAT over the mask over a 30 day period is collected from January 1-30 in 2009. The data are then placed onto a recta-linear map, and the data are gridded onto a 0.5 $\times$ 0.5 degree latitude/longitude resolution of mean values

for each square on the grid, as seen in Fig. A.2. To compare the spatial bias with another sensor, data from OSCAT-2 from January 1-30 in 2017 are also gridded in the same manner, as seen in Fig. A.3. Vertically polarized (V-pol) σ^0 are used, and only ascending passes from both sensors are used to minimize diurnal differences between the sensors [13]. To illustrate the differences in the spatial gradient between the sensors, a difference image is provided in Fig. A.4. The difference image shows that the spatial gradient of σ^0 between both sensors is within plus or minus 1 dB.

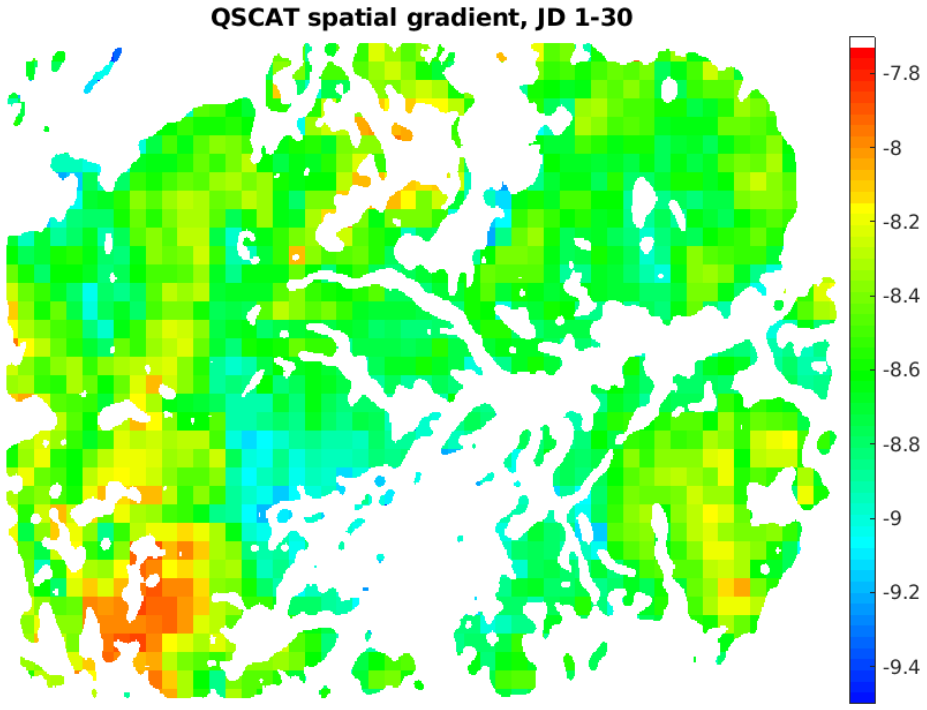

Figure A.2: QSCAT- V-pol data from JD 1-30 of 2009 collected and placed onto a recta-linear map. The color bar denotes σ^0 in dB. The measurements are gridded onto a 0.5 x 0.5 degree lat/lon resolution of mean values.

.

A.4 Azimuth Bias at Different Sections of the Gradient

To show the geographic consistency of the entire region, the mask is split up into 3 regions of interest along the spatial gradient as seen in Fig. A.5. Region 1 contains the center of the mask

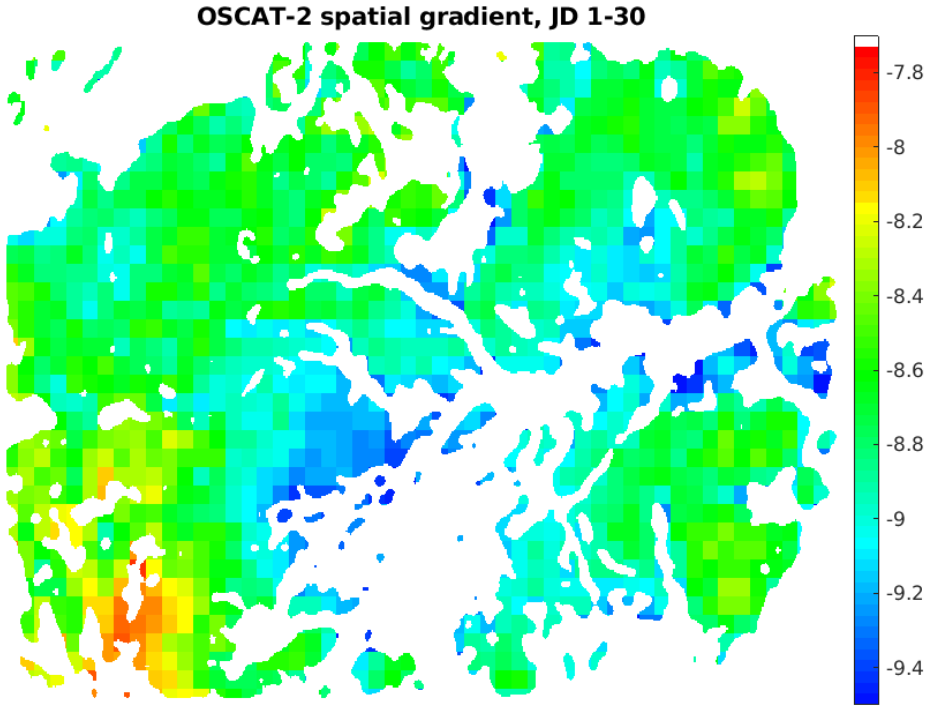

Figure A.3: V-pol σ^0 measurements processed as in Fig. A.2 for the OSCAT-2 scatterometer. The color bar denotes σ^0 in dB.

which is near the Amazon rivers, containing the lowest σ^0 values across the gradient in both the QSCAT and OSCAT-2 grids. Region 2 is the top half of the mask which is the most homogeneous region, or mostly the mean σ^0 of the area. Region 3 is the bottom half of the mask and contains both the highest and lowest σ^0 within the gradient. The high biased σ^0 are located in the terra firme areas in the southwest of the mask, while the low σ^0 are contained in the Amazon river. It is suggested that the terra firme cause the high spatial bias since that area contains regions with larger leaf sizes, according to Malhado et al. [23].

The spatial gradient does not introduce any bias into the QSCAT data as seen in Fig. A.6.

A.5 Summary

Despite having a spatial gradient on the order of 1 dB, the Amazon mask is consistently isotropic with respect to antenna azimuth angle and can therefore be used for scatterometer land

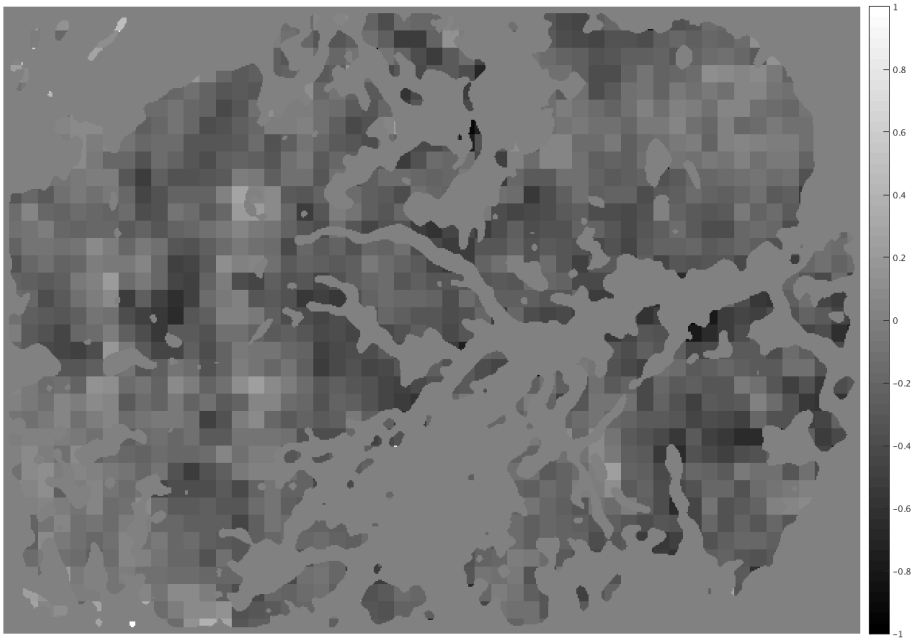

Figure A.4: Difference image of QSCAT and OSCAT-2 (Figs. A.2 and A.3) on a coarse grid resolution. The difference in σ^0 between the sensors is within plus or minus 1 dB.

calibration. The antenna azimuth bias of OSCAT-2 is not geographic, but consistent across different areas of the Amazon mask that both include and exclude both the minima and maxima of the spatial gradient. It is suggested that the spatial bias may stem from larger leaf sizes in specific areas such as terra firme reported by Malhado et al. [23].

QSCAT has no bias for σ^0 with respect to azimuth angle. For OSCAT-2, an antenna azimuth bias is consistent across areas of the spatial gradient, suggesting an instrumental bias of σ^0 with respect to the antenna azimuth.

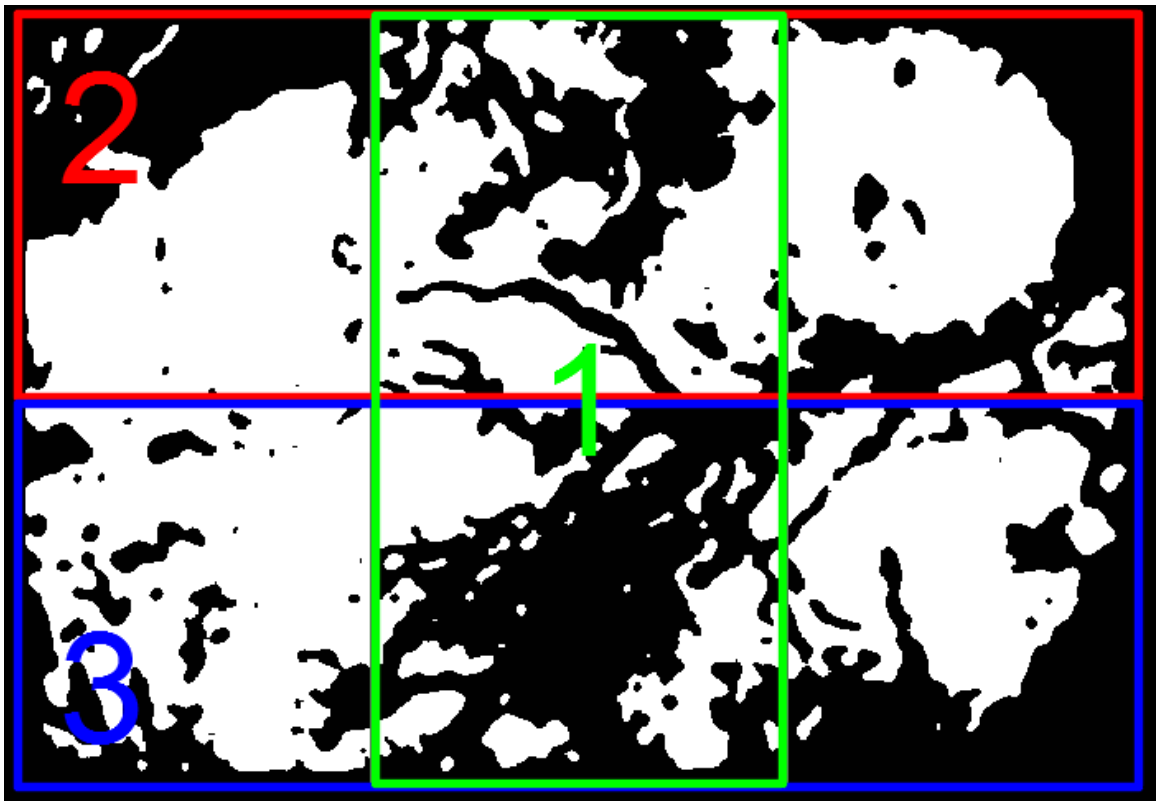

Figure A.5: The Amazon mask is split up into 3 regions: 1) Center, 2) Top, 3) Bottom. These regions include and exclude various regions along the mask that exhibit more and less geographic homogeneity.

.

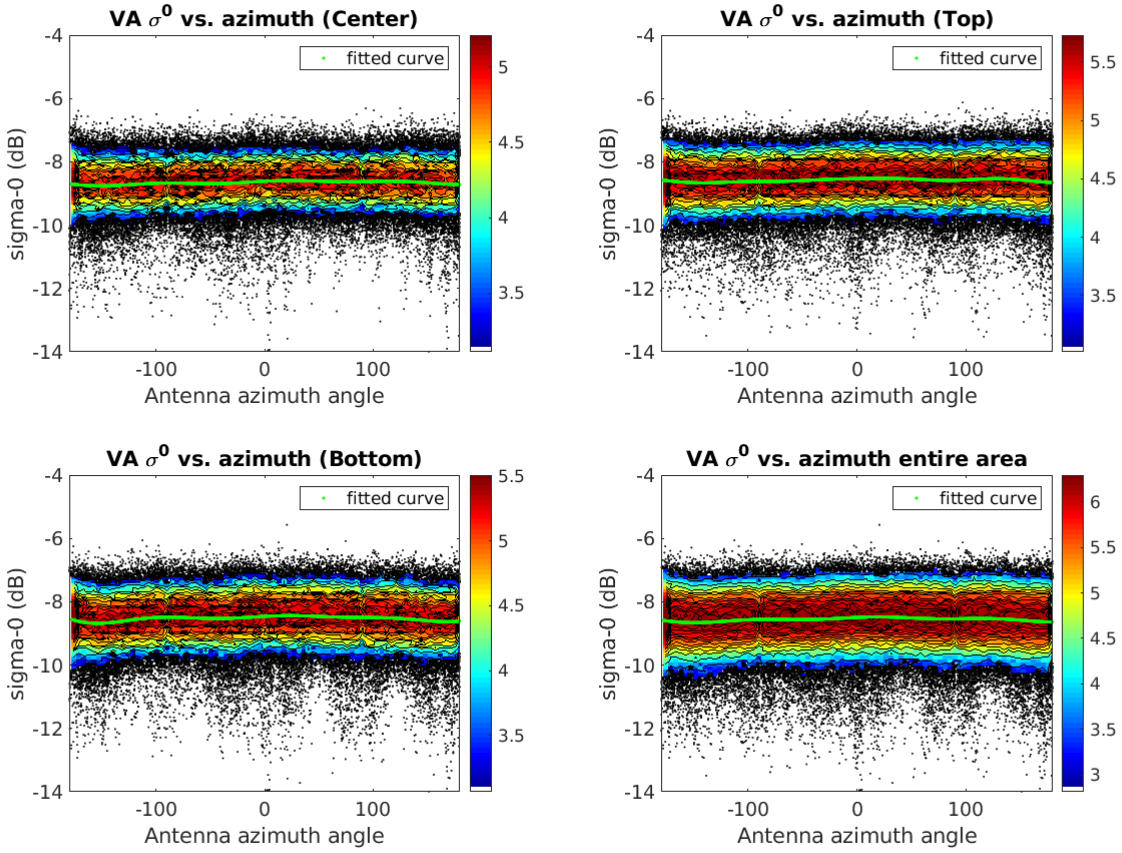

Figure A.6: QSCAT shows a consistent, unbiased σ^0 across all regions of the mask despite the southwestern corner exhibiting a spatial gradient

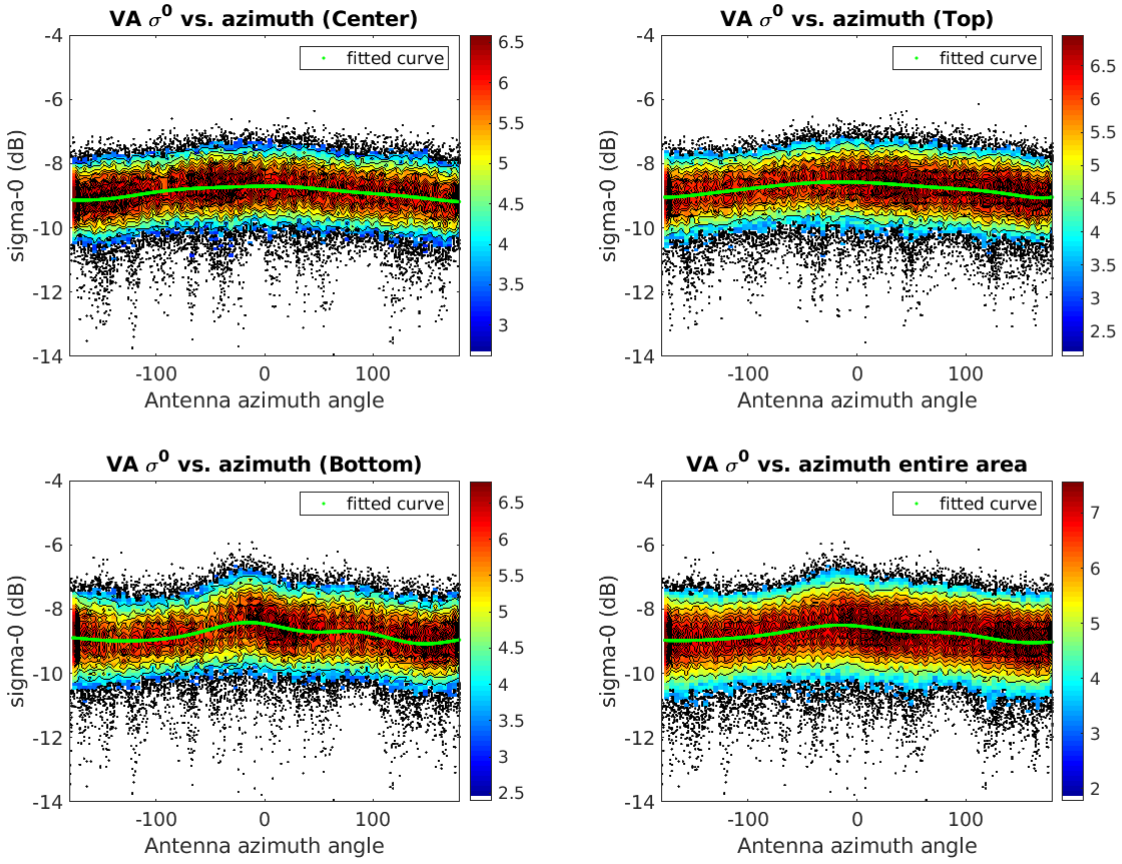

Figure A.7: OSCAT-2 has a consistent bias at the center azimuth angle near 0 degrees. The Center and Top regions exclude the highest point of the gradient in the southwestern corner of the mask and they still exhibit a similar, consistent azimuth bias